UNIVERSIDADE D
COIMBRA

SANDESH PRASAD ITANI

Mg-Zr SPUTTERED COATINGS: TOWARDS A BIODEGRADABLE MATERIAL FOR TEMPORARY BONE IMPLANTS

VOLUME 1

Dissertation under the Joint European Master's Degree in Surface Tribology and Interfaces guided by Prof. Dr. Sandra Carvalho and Prof. Dr. Ana Sofia Ramos presented to the Department of Mechanical Engineering of the Faculty of Science and Technology of the University of Coimbra

July 2023

1 2 9 0

FACULDADE DE CIÊNCIAS E TECNOLOGIA
UNIVERSIDADE D COIMBRA

Mg-Zr Sputtered Coatings: Towards a Biodegradable Material for Temporary Bone Implants

Submitted in Partial Fulfilment of the Requirements for the Degree of European Joint European Master in Tribology of Surfaces and Interfaces.

Revestimentos Mg-Zr: Rumo a um Material Biodegradável para Implantes Ósseos Temporários

Author

Sandesh Prasad Itani

Advisor[s]

Prof. Dr. Sandra Carvalho
Professor at University of Coimbra
Prof. Dr. Ana Sofia Ramos
Professor at University of Coimbra

Jury

President	**Prof. Dr. Bruno Trindade** **Professor at University of Coimbra**
Vowel	**Prof. Dr. Filipe Fernandes** **Assistant Professor at Polytechnic of Porto**
Advisor	**Prof. Dr. Ana Sofia Ramos** **Professor at University of Coimbra**

· U C ·

UNIVERSIDADE DE COIMBRA

tribos
Joint European Master in Tribology of Surfaces and Interfaces
Ljubljana • Leeds • Coimbra • Luleå

Coimbra, July 2023

ACKNOWLEDGEMENTS

I would like to express my sincere appreciation for the constant support and guidance provided by my supervisors, Prof. Sandra Carvalho, and Prof. Ana Sofia Ramos. They have been instrumental in helping me complete this project and have provided valuable ideas to overcome the obstacles I encountered during my scientific research. I would also like to acknowledge the contributions of Jose David Castro, Dr. Zohra Benzarti, Daniela Santo, Dr. Diogo Cavaleiro, Dr. Todor Vuckov, Prof. Albano Cavaleiro, Dr. Pooja Sharma, Dr. Ricardo Serra, and the technical staff at Institute Pedro Nunes who have assisted me throughout this research.

I am grateful for the support and guidance from professors, lecturers, and colleagues at the University of Leeds, University of Ljubljana, and University of Coimbra. Their input has been invaluable on this journey. I would like to thank the TRIBOS consortium for selecting me and providing me with the opportunity to gain in-depth knowledge in the field of tribology.

Lastly, I want to express my heartfelt thanks to my family for their constant motivation and support throughout this journey.

RESUMO

As ligas de magnésio (Mg) têm sido alvo de extensa investigação quanto ao seu potencial uso como materiais biodegradáveis em implantes ósseos temporários. A crescente popularidade dos implantes à base de magnésio pode ser atribuída à sua compatibilidade com o osso humano, baixo módulo de Young e capacidade de mitigar os efeitos de "stress shielding" comumente associados aos implantes ósseos permanentes. O zircônio (Zr), um elemento de liga biocompatível e não tóxico, é comumente utilizado para melhorar as propriedades mecânicas e de resistência à corrosão do magnésio. Neste estudo, a técnica de pulverização catódica dc magnetrão foi utilizada para produzir revestimentos de Mg-xZr (x=0,0-5,0 at.%). Os revestimentos foram submetidos a várias técnicas de caracterização física, química, estrutural, de superfície, eletroquímica e tribológica, incluindo microscopia eletrónica de varrimento (MEV), espectroscopia de dispersão de energia dispersiva, difração de raios X (DRX), microscopia de força atómica, nanoindentação, polarização potenciodinâmica (PP), espectroscopia de impedância eletroquímica (EIE) e tribómetro alternativo.

A análise MEV revelou que os filmes exibiram crescimento colunar com vazios, enquanto um aumento no teor de Zr resultou no refinamento de grão e na formação de filmes mais densos. A análise de DRX indicou a presença do plano basal Mg (00.2), que se tornou mais pronunciado com a dopagem de Zr, enquanto os picos exibiram um deslocamento gradual para ângulos mais elevados. Este desvio foi atribuído ao menor tamanho atómico do Zr dentro da rede cristalina do Mg, resultando numa redução do parâmetro de rede "c" e num aumento no parâmetro "a". Testes de molhabilidade demonstraram o comportamento "liquifílico" dos revestimentos Mg-Zr, indicando a sua compatibilidade com o fluido corporal sintético . A análise de nanoindentação revelou um aumento de dureza dos revestimentos à medida que o teor de Zr aumentou. No entanto, os revestimentos Mg-0,4Zr e Mg-1,0Zr exibiram menor dureza em comparação com o magnésio puro. Esta diminuição de dureza pode ser atribuída à maior taxa de deposição, o que resultou num aumento de vazios e consequente diminuição da compacidade destes revestimentos.

Os testes de PP revelaram melhor resistência à corrosão nos revestimentos Mg-Zr com teores de Zr entre 1,0 e 3,4 %at. Estes resultados foram suportados por imagens de MEV. Os resultados do EIE mostraram que os revestimentos de Mg-Zr se comportaram como um circuito de Randles simples no diagrama de circuito elétrico equivalente. Embora os revestimentos de Mg-Zr tenham apresentado uma elevada taxa de desgaste, o coeficiente de atrito médio foi reduzido em comparação com o substrato. Além disso, a taxa de desgaste dos revestimentos Mg-Zr diminuiu com o aumento do teor de Zr na matriz de Mg. Em conclusão, a adição de Zr ao magnésio melhorou a sua resistência à corrosão e as suas propriedades mecânicas, tornando-o um material biodegradável promissor para potenciais aplicações em implantes ósseos temporários.

Palavras-chave Magnésio, zircónio, pulverização catódica magnetrão, revestimentos Mg-Zr, corrosão, tribologia

ABSTRACT

Magnesium (Mg) alloys have undergone extensive investigation due to their potential use as biodegradable materials in temporary bone implants. The rising popularity of magnesium-based implants can be attributed to their compatibility with human bone, low Young's modulus, and ability to mitigate stress-shielding effects commonly associated with permanent bone implants. Zirconium (Zr), a biocompatible and non-toxic alloying element, is commonly utilized to enhance the mechanical and corrosion resistance properties of magnesium. In this study, the Direct Current Magnetron Sputtering (DCMS) technique was employed to fabricate Mg-xZr (x=0.0-5.0 at. %) coatings. These coatings were subjected to various physical, chemical, structural, surface, electrochemical, and tribological characterization techniques, including scanning electron microscopy (SEM), energy dispersive spectroscopy (EDS), X-ray diffraction (XRD), atomic force microscopy (AFM), nanoindentation, potentiodynamic polarization (PP), electrochemical impedance spectroscopy (EIS), and reciprocating tribometer.

SEM analysis revealed that the films exhibited columnar growth with voids, while an increase in Zr content resulted in grain refinement and the formation of denser coatings. XRD analysis indicated the presence of the Mg (00.2) basal plane, which became more pronounced with Zr doping, while displaying a gradual shift of the peaks towards higher angles. This shift was attributed to the smaller atomic size of Zr within the Mg crystal lattice, resulting in a reduction of the "c" lattice parameter and an increase in the "a" parameter. Wettability tests demonstrated the "liquiphilic" behaviour of the Mg-Zr coatings, indicating their compatibility with plasma simulated body fluid (SBF). The nanoindentation analysis revealed an increase in the hardness of the coatings as the Zr content increased. However, Mg-0.4Zr and Mg-1.0Zr coatings exhibited lower hardness compared to pure magnesium. This decrease in hardness can be attributed to the higher deposition rate, which resulted in an increase in voids and a decrease in compactness within these coatings.

PP tests revealed better corrosion resistance of the coatings with Zr contents from 1.0 to 3.4 at. %. These findings were further supported by SEM imaging. EIS results illustrated that the Mg-Zr coatings behaved like a simple Randles circuit in the equivalent electric circuit diagram. Although the Mg-Zr coatings exhibited a high wear rate, the average coefficient of friction (COF) was reduced compared to the substrate. Furthermore, the wear rate of the Mg-Zr coatings decreased with an increase of the Zr content in the Mg matrix. In conclusion, the addition of Zr to magnesium improved its corrosion resistance and mechanical properties, making it a promising biodegradable material for potential applications in temporary bone implants.

Keywords Magnesium, zirconium, magnetron sputtering, Mg-Zr coatings, corrosion, tribology

Contents

List of Figures

List of Tables

List of Abbreviations

List of Symbols

γd – Dispersive surface free energy
γp – Polar surface free energy
γt-Total surface free energy
R_{coat}- Charge transfer resistance/Coating resistance
$|Z|$- Modulus of impedance
$-Z_{img}$- Impedance in imaginary axis
Z_{real}- Impedance in real axis
R_{sol}-Solution resistance
α- Constant phase exponent
β_{a-} Anodic slope
β_{c-}Cathodic slope
J_{corr-} Corrosion current density
E_{corr-} Corrosion potential

List of Acronyms

Mg-Magnesium
Zr- Zirconium
Zn-Zinc
Al-Aluminium
Ca-Calcium
Na-Sodium
P-Phosphorous
Fe-Iron
Cr-Chromium
Cl-Chlorine
Ti-Titanium
Mn-Manganese
Sr-Strontium
Sn-Tin
Sc-Scandium
Y-Yttrium
Nd-Neodymium
Gd-Gadolinium
Ce- Cerium
La- Lanthanum
Si-Silicon
O-Oxygen
SS- Stainless Steel
REE-Rare Earth Element
SBF-Simulated Body Fluid
DC-Direct Current
RF-Radio Frequency
UTS-Ultimate Tensile Strength
DCMS- Direct Current Magnetron Sputtering
3D-Three Dimension
2D-Two Dimension
EIS-Electrochemical Impedance Spectroscopy
CPE- Constant Phase Element

PA-Phase Angle
PP- Potentiodynamic Polarization
CR-Corrosion Rate
SEM-Scanning Electron Microscope
XRD-X-Ray Diffraction
HCP-Hexagonal Closed Packed
FWHM- Full Width Half Maximum
EDS- Energy Dispersive X-ray Spectroscopy
AFM-Atomic Force Microscope
CEMMPRE-Centre for Mechanical Engineering, Materials and Processes
IPN-Instituto Pedro Nunes
SFE-Surface Free Energy
BNF-Bromonaphthalene
DM-Diiodomethane
EG-Ethylene Glycol
H-Hardness
E-Young's Modulus
Er-Reduced Young's Modulus
SiN-Silicon Nitride
COF-Coefficient of Friction
XPS-X-ray Photoelectron Spectroscopy
TEM-Transmission Electron Microscopy

1. Introduction

1.1 Motivation

Metallic materials continue to have a crucial role in the field of biomaterials, aiding in the treatment of diseased or damaged bone tissue. Their high mechanical strength and fracture toughness make metals more suitable than ceramics or polymers for load-bearing applications. Commonly used metallic biomaterials, such as stainless steels, titanium, and cobalt-chromium-based alloys, have gained approval but possess limitations. These limitations involve the potential release of toxic metallic ions or particles through corrosion or wear processes, which trigger inflammatory reactions, reduce biocompatibility, and cause tissue loss. Additionally, the Young's moduli of current metallic biomaterials do not align well with natural bone tissue, leading to stress shielding effects that hinder the stimulation of new bone growth and remodelling, thereby compromising implant stability [1].

In recent years, biodegradable biomaterials, particularly magnesium alloys, have gained interest for medical use. These materials must meet specific requirements: good biocompatibility and appropriate mechanical properties for fracture healing. Magnesium is an essential component in the human body, stored mainly in bones and utilized by enzymes for various reactions. Magnesium's mechanical properties closely resemble those of natural bone, making it a promising alternative to titanium alloys [2].

However, the rapid degradation of Mg in vivo can lead to premature failure of implants, limiting its use in practical applications. When magnesium and its alloys corrode, they release hydrogen gas. However, the rapid production of large amounts of gas is undesirable for clinical purposes. The amount of gas generated is closely linked to the corrosion rate [2]. Corrosion is a type of biodegradation. The biodegradability of magnesium is its greatest advantage, but the rapid degradation rate is its main drawback. In a physiological environment, magnesium degrades quickly, which can undermine its mechanical strength and integrity in various applications. Additionally, this accelerated degradation can lead to harmful consequences, including premature implant failure, interference with the healing process, and, in severe cases, even death [3].

The aim of this master thesis is to use DC magnetron sputtering as a predictive technique to find the optimum chemical composition of Mg-Zr that shows minimum corrosion, which can be later developed using 3D printing in bulk form for biomedical implants. DC magnetron sputtering is a widely used physical vapour deposition technique that allows for the deposition of thin films with precise composition control. This technique is suitable for the rapid screening of many Mg-Zr chemical compositions, which can significantly reduce the time and cost involved in alloy development. Magnesium based biodegradable implants are shown in figure 1a and 1b.

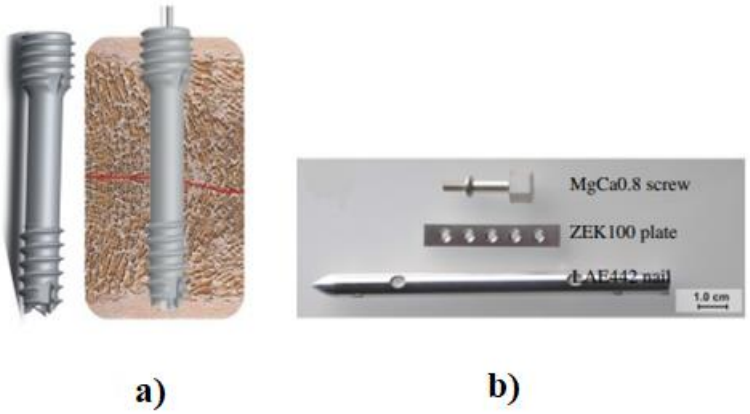

Figure 1: Mg-based biodegradable implants: a) MAGNEZIX screw; [4] and b) biodegradable implants for orthopaedics application [2].

1.2. Research gap of the thesis

Mg-based temporary bone implants pose challenges due to their high degradation rate, leading to implant failure prior to complete bone regeneration. To address this issue, extensive research has been conducted on alloying Mg-based implants with elements such as zinc, zirconium, strontium, and rare earth metals to mitigate their significant corrosion rates. These investigations have primarily involved the fabrication of Mg-based bone implants using conventional techniques like casting and rolling, as well as innovative approaches like laser additive manufacturing, which limits the solubility of Mg and alloyed elements. The corrosion resistance of these implants is largely determined by the maximum solubility of these alloying elements in magnesium. In the form of coatings, it is possible to test several chemical compositions using small quantities of material. Furthermore, by adjusting the deposition parameters, it becomes possible to obtain a range of magnesium-based alloy compositions, an opportunity not readily available with traditional methods. In this work, the impact of different zirconium alloying contents on the corrosion rate, mechanical properties and tribological behaviour of Mg-based coatings is examined.

The corrosion behaviour of films with different chemical compositions is compared with the aim of identifying the optimal zirconium content that effectively controls corrosion while enhancing mechanical and tribological performance.

1.3. Objectives

The primary objective of this work is to utilize DC magnetron sputtering as a predictive technique to produce corrosion-resistant Mg-Zr coatings. These coatings aim to achieve an optimal chemical composition suitable for the development of biodegradable and biocompatible bone implants through 3D printing. The experimental approach involved employing a DC magnetron sputtering process, with stainless steel 316L and silicon serving as substrates, and magnesium and zirconium as target materials. To accomplish the main objectives, the following specific goals were achieved:

- Deposition of Mg-based coatings using DC magnetron sputtering with varying zirconium contents.
- Investigation of the morphology, chemical composition, and crystal structure of the coatings, utilizing SEM, EDS, and XRD techniques. This analysis aimed to establish a correlation between zirconium concentration in the coatings and their respective properties.
- Evaluation of the mechanical properties of the coatings by nanoindentation.
- Exploration of the impact of zirconium on corrosion inhibition by measuring the corrosion rate of the coatings with different zirconium contents.
- Disclosure of the corrosion behaviour of Mg-based coatings, with the objective of identifying the chemical composition that exhibits the lowest degradation rate.
- Performance of tribological characterization to determine the wear rate and COF of the Mg-Zr coatings which exhibit good corrosion resistance.

1.4. Thesis structure

The proposed research work is a master's thesis for the Joint European Masters in Tribology of Surfaces and Interfaces and is entitled "Mg-Zr sputtered coatings: Towards a biodegradable material for temporary bone implants." The aim of this work is to employ DC magnetron sputtering to develop Mg-based coatings containing Zr in small quantities and investigate the impact of Zr on the coatings' mechanical properties, as well as on corrosion and tribological behaviour for potential use in temporary bone implants. The thesis report is divided into five major sections: introduction, state of the art, experiment procedure, results and discussion, and conclusions.

The introduction includes motivation, research gap of the thesis and objectives. The state of the art is emphasized on magnesium alloys and their applications, Mg-based bone implants, causes of failure of Mg-based implants, improvements of their properties, corrosion behaviour, corrosion-resistant strategies, and DC magnetron sputtering. The experimental procedure has a description of all tasks that were carried out, which includes the development of coatings and characterization techniques involved in the process. The results and discussion section focuses on various results obtained from different characterization and experiments. The conclusions include summary of the results and future works which can further expand knowledge of current work.

2. State of The Art

2.1. Magnesium alloys and their applications

Magnesium is alkaline in nature and has a bright, silvery-white look. Due to its highly reactive nature, it is not found free in nature [3]. With a density of 1.74 g/cm^3, it is also the lightest engineering metal and, in comparison to steel and aluminium, exhibits a higher strength-to-weight ratio and better castability [3], [5]. The main weakness of magnesium is its high corrosion rate, which can be brought on by strong electrolyte species or by the presence of metallic contaminants [3]. Since alloying elements can significantly improve the physical properties of Mg-based alloys, magnesium must be alloyed for engineering applications to lessen its corrosive nature and improve mechanical properties [3].

Two often utilized alloying elements are aluminium and zinc, with aluminium typically serving as the foundation for alloys based on magnesium. Each is affordable and very soluble in magnesium [6]. The addition of zinc improves the alloy's dimensional stability and fluidity during casting. The corrosion resistance of Mg-Zn alloy is increased when it combined with additional impurities like nickel and iron [7]. Al, Zn, Mn, Ca, Zr, Sr, and Sn, as well as rare earth (RE) metals like Nd and Gd, enhance corrosion resistance when alloyed with magnesium. However, the maximum solubility of these elements in magnesium determines the corrosion resistance; therefore, adding more than the maximum solubility may not increase magnesium corrosion resistance. The strongest and ductile alloys are Mg-RE-based, whereas Mg-Zn-based alloys have outstanding ductility and corrosion resistance. Additionally, the least ductile and strong alloys are those based on magnesium and Zr [8]. Mg-based alloys are particularly used in aerospace industry, automotive industry and in biomedical industry as biomaterial. In figure 2, various families of magnesium alloys are shown while yield strength with respect to strain at failure of several Mg-based alloys is shown in figure 3.

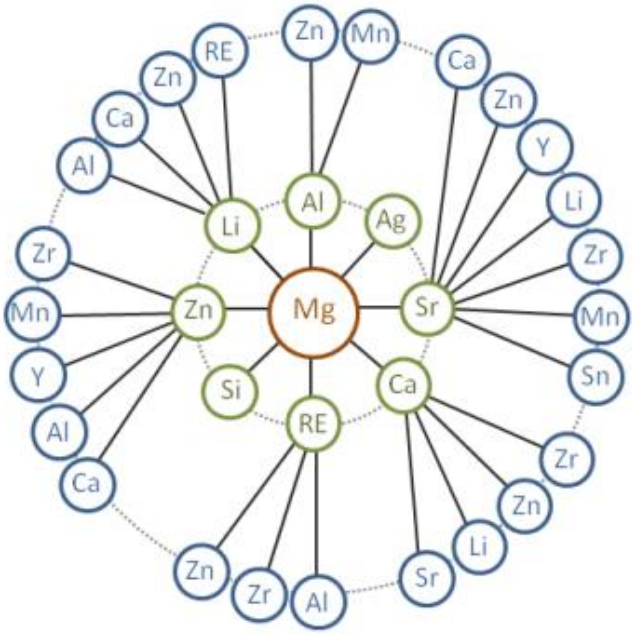

Figure 2: Main families of magnesium alloys (binary and tertiary systems) [9].

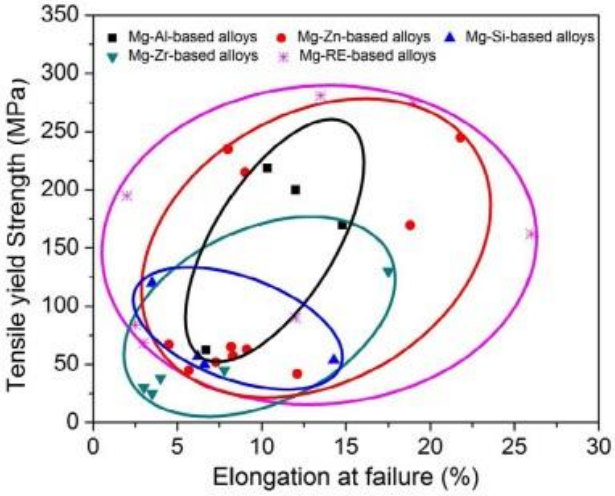

Figure 3: Yield strength vs elongation at failure of Mg alloys [8].

Magnesium is also used in aerospace industry due to its superior machinability, castability, and low density; magnesium has been utilized in aircraft parts since World War II [10]. If magnesium-based alloys are used instead of aluminium-based alloys in aircraft, the overall weight of the aircraft can be reduced up to 60.4 tonnes, which is equivalent to 28% of its "operating empty weight" [11]. Mg-based alloys are the third most often used material in the automotive sector since they are employed in the engines, chassis, and body structures of cars [12]. The demand for magnesium-based alloys has increased because of the widespread notion of sustainable development, which has increased pressure from authorities to reduce emissions and environmental impact. This can be achieved by lightening the weight of vehicles and using less energy without sacrificing strength and functionality [3], [5].

2.1.1. Applications as biomaterial

Magnesium has numerous uses in the biomedical and healthcare industries. Magnesium was initially applied in medicine by Edward C. Huse in 1878, when he employed Mg wires to bind blood vessels [3]. Numerous magnesium screws, plates, sheets, wires, and tubes have undergone testing on both people and animals [13]. Magnesium is increasingly in demand as a biomaterial, particularly for use in temporary bone implants. Magnesium-based materials are advantageous for use as bone implants since they are biocompatible with bone and non-toxic due to their natural occurrence inside the human body [14]. Additionally, Mg is a vital metal needed for human body to assist in the structural stabilization of nucleic acids, cell membranes, and proteins [15]. One of the desired characteristics of the temporary bone implant is that it is biodegradable and will dematerialize after the tissue has fully recovered. The bone implant that is biodegradable should lose its mechanical toughness and stiffness at an inversely proportional rate as compared to bone healing. Bone implants made of magnesium can also promote bone growth [16]. Unlike conventional metallic implants made of stainless steel, cobalt-chromium, or titanium-based alloys, which are mostly bioinert, magnesium is biodegradable and bioabsorbable. As a result, as the bone regenerates, there is no requirement for additional surgery to remove the implant [17]. Figure 4 illustrates the use of Mg-based screws in orthopaedics.

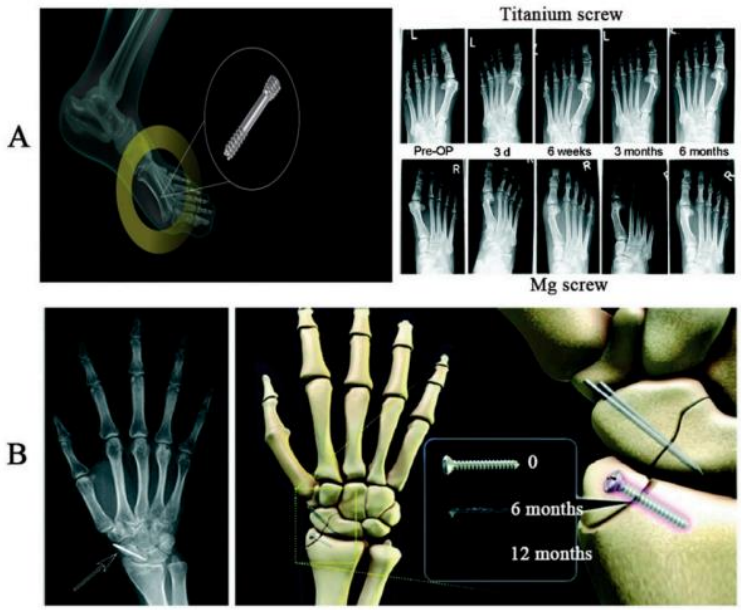

Figure 4*:* Use of magnesium in orthopaedics [3].

2.2. Magnesium-based bone implants

Magnesium can be regarded as a biomaterial because it is the fourth most common element in the human body and is crucial to human metabolism. It functions as a coenzyme and aids in the stability of DNA and RNA structures. Magnesium is an appealing material for bone implants due to its high fracture toughness when compared to hydroxyapatite, low density, and an elastic modulus close to the human bone [18]. These days, there is a growing demand for biodegradable implants. A temporary bone implant should have mechanical strength, biocompatibility, osteopromotive characteristics, and an optimum degradation rate [19]. Bone implants made of magnesium have low Young's modulus (35–45 GPa) and low density (1.78–2.0 g/cm^3) that are similar to human bone [20]. This reduces the likelihood of a stress shielding effect on bones [20]. Additionally, magnesium has good formability, castability, and machinability, all of which facilitate production [20]. One of the desired characteristics of temporary bone implants is that implants made of magnesium dissolve in living tissue, avoiding the need to remove the implants through a second operation, which would add to the patient's discomfort and cost burden [19]. The human body requires a daily intake of approximately 21 to 28 grams of Mg to support its normal physiological processes. Magnesium plays a crucial role in the formation of both bone and soft tissues. The body is protected from adverse effects by excretion of excess levels from urine [19].

The release of magnesium ions aids in the production of CGRP (calcitonin gene-related peptide), which in turn causes proteins to bind to cyclic adenosine monophosphate, raising osteoblasts and promoting the development of new bone [19]. Magnesium also plays a significant part in osteopromotion. Magnesium-based implants can be employed for bone fixation and as a bone scaffold for tissue regeneration despite their high rate of disintegration [19]. The presence of magnesium-based thin film metallic glasses in bone implants reduced differences at the bone-implant interface [21]. Figure 5 shows stiffness vs time graph of healing bone and temporary bone implant.

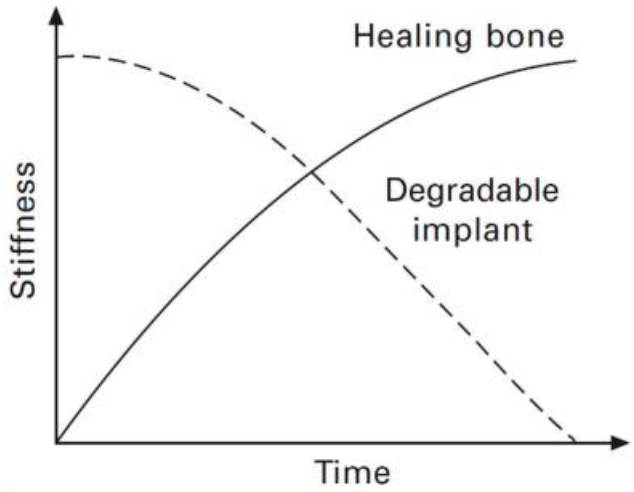

Figure 5: Graph indicating stiffness vs healing time of biodegradable implant [3].

2.3. Cause of failure of magnesium-based bone implants

Due to magnesium's fast deterioration rate and low standard electrode potential of -2.37 volts, Mg-based implants frequently fail [22]. This causes an early loss of the implant's mechanical capabilities and the in vivo development of hydrogen gas, which causes tissue swelling and an increase in alkalinity at the implant site [19]. To mimic the bone's natural repair process, the Mg-based implant's deterioration rate should be between 0.2 and 0.5 mm annually [23]. In the 3-6 month-long reconstruction phase of the implant, the damaged bone tissue is stimulated by increasing load to return the bone's load-carrying capacity to its pre-injury state. However, due to the rapid degradation of magnesium caused by pitting corrosion, implants corrode before the reconstruction phase, creating a significant barrier to the repair of bone tissue [24]. The three main reasons for the failure of Mg-based implants are the creation of H_2 gas, anodic and cathodic site formation in implants, and pit formation. Hydrogen gas builds up under the skin, which causes implants to become hydrogen embrittled and fail. This partially causes the existence of hydroxyl groups and an elevation in pH in the surrounding tissue, which prevents the development of new tissue and cell growth.

The production of hydrogen bubbles significantly impairs tissue healing in the surgical site, because the formation of gas pockets causes the separation of tissues and tissue layers due to necrosis of tissue. A magnesium-based implant that has had excessive corrosion may experience local alkalization, which raises the pH level above 7.8 in the area around the implant and causes alkaline poisoning [25].

2.4. Corrosion behaviour of Mg-based bone implants

Corrosion in magnesium can be uniform or localized corrosion [3]. In physiological fluid degradation reaction of magnesium-based alloys is given below [2]:

Anodic reaction: $$Mg \rightarrow Mg^{2+} + 2^{e-}$$
Cathodic reaction: $$2H_2O + 2^{e-} \rightarrow H_2 \uparrow + 2OH^-$$
$$Mg^{2+} + 2OH^- \rightarrow Mg(OH)_2(s)$$

The rapid rate of corrosion of a Mg-based implant in the presence of an electrolytic physiological environment is one of its main drawbacks. Magnesium in the unprotected

atmosphere will form a grey oxide coating of magnesium hydroxide ($Mg(OH)_2$), which slows the pace of corrosion. The formation of highly soluble magnesium chloride and hydrogen gas results in pitting corrosion of Mg-based bone implants, while serious corrosion also occurs in the presence of chloride ions up to a concentration of 150 mmol/l. The overall reaction can be summarized as follows [1]:

$$Mg(s) + 2H_2O \rightarrow Mg(OH)_2(s) + H_2(g) \uparrow$$
$$Mg(s) + 2Cl^-(aq) \rightarrow Mg(Cl)_2$$
$$Mg(OH)_2(s) + 2Cl^-(aq) \rightarrow Mg(Cl)_2$$

As bacteria are killed by concentrations of magnesium and hydroxyl ions, which in turn depend on the rate of magnesium degradation, biodegradable implants made of magnesium can benefit from this corrosive characteristic of Mg-based alloys. Therefore, antibacterial properties of Mg-based alloys are superior to those of bio metals like titanium [26]. Magnesium-based alloys are lightweight, have a good strength-to-weight ratio, and have limited corrosion resistance in aqueous solutions with low and medium hydrogen ion concentrations (pH) [27]. By regulating its microstructure and precipitates, which are crucial for the deterioration of magnesium alloy, it is possible to manage the corrosion behaviour of magnesium [27].

2.5. Strategies for corrosion-resistant bone implants

Numerous processes can be used to fabricate temporary bone implants made of magnesium. The way the bone implants are made has a direct impact on their mechanical characteristics, rate of corrosion, and effectiveness inside the human body. Casting, powder metallurgy, and additive manufacturing are used to make bone implants made of magnesium. Purification, alloying of implants containing magnesium, surface coating, and metal matrix composites of magnesium are the four basic methods for reducing the rate of deterioration of magnesium [28].

Galvanic corrosion of the implant can be reduced by lowering the limit of the second phase in the Mg matrix, which can be done using purification method in Mg-based alloys [29]. The content of impurities like iron, copper, and nickel in the Mg matrix affects the rate of corrosion of magnesium-based alloys; the rate of corrosion is reduced when the amount of these impurities is below the tolerance limit. When the amount of iron is less than 26 ppm, the corrosion rate of Mg is lowered from 14.9 mm/year to 0.5 mm/year [28].The corrosion resistance of the implants is greatly increased by adding alloying elements to the magnesium matrix [30]. When Mg is alloyed, its mechanical and corrosion properties are enhanced, which helps in the proper healing of bones [31].

One method for preventing the degradation of implants made of magnesium is surface coating, which aids in separating the magnesium matrix from bodily fluid [32]. Calcium stearate based superhydrophobic coating exhibit higher corrosion resistance compared to bare magnesium and Plasma Electrolytic Oxidation pre-treated magnesium [33]. The corrosion resistance of hydroxyapatite coatings on bulk WE43 Mg-based alloy is higher when fabricated using pulsed laser deposition than electrophoretic deposition, with corrosion rates of 0.073 mm/year and 0.194 mm/year, respectively [34]. Akermanite ($Ca_2MgSi_2O_7$) coating in nanostructure form exhibits better corrosion resistance behaviour and improves the bioactivity of Mg-based biodegradable implants [35]. In an electrochemical test using plasma SBF (Simulated Body Fluid) at 37 ºC, polycaprolactone and polylactic acid coated pure magnesium showed a lower corrosion rate than uncoated

pure magnesium [36].

Corrosion resistance of Mg-based metal matrix composites can be improved by controlling the reinforcement which are bioactive bio ceramics [32]. Graphene oxide reinforcement in the α-Mg matrix of AZ61 alloy was used to develop the AZ61-1 wt.% graphene oxide alloy, which improved the corrosion resistance and cytocompatibility of the existing AZ61 alloy. This is a result of the dispersion of graphene oxide particles at grain boundaries, which create a honeycomb nanostructure surrounding the α-Mg grains [37]. Figure 6 shows various techniques to regulate corrosion behaviour of Mg-based alloys.

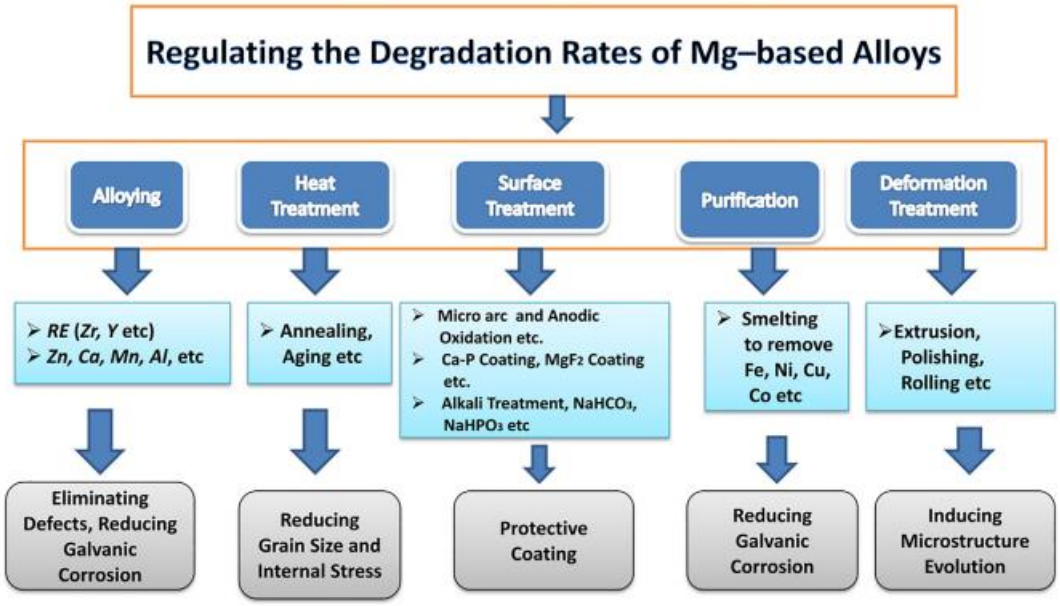

Figure 6: Various strategies to regulate corrosion rate of Mg-based alloys [31].

2.6. Improvement of properties of Mg-based bone implants

To enhance the qualities of Mg-based bone implants, many strategies have been used. Most of them are concerned with slowing down the excessive pace of magnesium deterioration, which causes implants to fail too soon. For Mg-based bone implants that resist to corrosion, alloying techniques are the mostly used. The development of intermetallic phases by alloying elements improves the corrosion resistance of Mg-based bone implants, increasing their mechanical and physical characteristics [38]. Zr, Zn, Ti, Ca, and rare earth metals are among the widely used elements for alloying of Mg-based alloys. The influence of these elements on the corrosion behaviour of Mg-based bone implants is described below:

2.6.1. Influence of zirconium

Zr offers strong corrosion resistance and biocompatibility in addition to minimal in vitro cytotoxicity. Additionally, it exhibits osteocompatibility that is on par with or even better than titanium. Zr is soluble in Mg up to 3.8 wt.% at ~ 650ºC. Alloys made of Mg, Zr, and Sr have good ductility and average strength. The Mg-1Zr-2Sr alloy demonstrates various desirable qualities, including in vivo and in vitro compatibility, corrosion resistance, and appropriate mechanical properties [39]. In Mg alloys, Zr functions as a grain refiner [18]. Due to limited solubility of Zr in the Mg matrix, crystallization is inhibited throughout

the solidification process. Undissolved Zr particles act as nucleation sites, resulting in the development of tiny equiaxed grains with a recognizable hexagonal shape. Additionally, Zr develops protective oxide films. When Mg-Zr alloy is submerged in borate buffer solution, it develops a Mg-Zr double hydroxide layer with Zr cations, which serve as corrosion inhibitors [40]. In recent studies, it has been found that the content of Zr in Mg should be less than 5 wt.%. Zr shows biocompatibility when alloyed with Sr and Ca in Mg-Zr-Sr and Mg-Zr-Ca alloys, respectively. The addition of Zr to Mg alloys reduces corrosion when its content is less than 2 wt.%, while there is a reduction in corrosion-resistant property when the amount is more than this [40].

Mg-0.5Zr-2Ca and Mg-1Zr-(1,2) Ca alloys comprise both α-Mg and Mg_2Ca phases. Mg-(0.5,1) Zr-(1,2) Ca alloys have low strength and poor ductility due to the formation of the Mg_2Ca phase along the grain boundaries, which plays a role in decreasing the strength [41]. However, addition of Sr and Sn to Mg-Zr-Ca alloys helps to improve corrosion resistance [42]. Figure 7 shows the influence of the addition of Zr and Sr on the microstructure of Mg-based alloys in comparison to pure Mg.

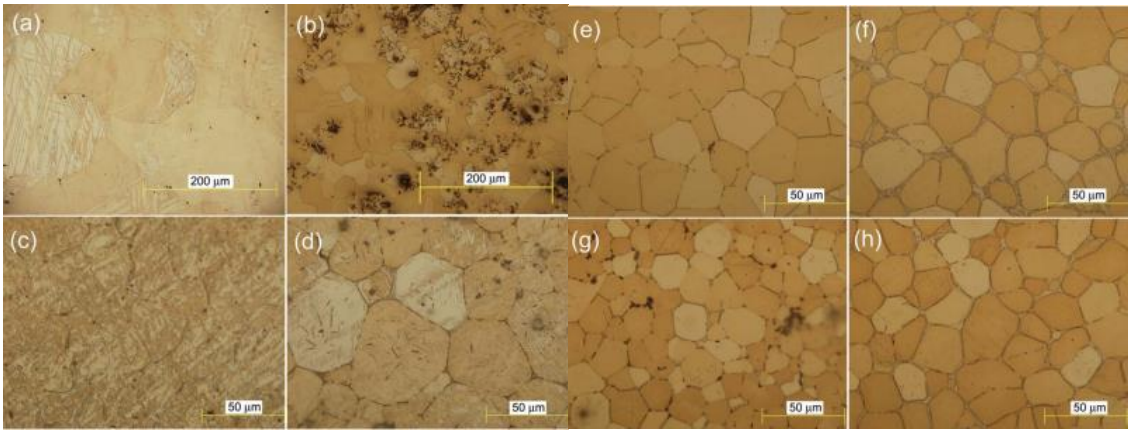

Figure 7: Microstructure of Mg-Zr-Sr alloys showing grain refinement: a) Mg; b) Mg–5Zr; c) Mg–1Zr–2Sr; d) Mg–1Zr–5Sr; e) Mg–2Zr–2Sr; f) Mg–2Zr–5Sr; g) Mg–5Zr–2Sr; and h) Mg–5Zr–5Sr [40].

By reinforcing the grain boundary, boosting mechanical characteristics, and lowering the alloy's rate of corrosion, the use of Zr in bone implants aids in the improvement of alloy strength [22]. When the amount of calcium is raised, the rate of corrosion and biocompatibility of Mg-Zr-Ca alloys are reduced [24]. When Zr is added to magnesium-based alloys, the alloys' corrosion resistance, compressive strength, and ductility all significantly increased; however, the elastic modulus of the Mg-Zr-Ca alloy decreases [24]. The ideal material, Mg-1Zr-1Ca, has the best biocompatibility, lowest corrosion rate, maximum compressive strength, and highest ultimate tensile strength (UTS) [24]. The Zr addition, which ranges from 0.1 to 0.2 wt.%, aids in the improvement of the alloy's microstructure and grain boundaries [22]. A minimum corrosion rate of 0.056 mm per year and 0.059 mm per year was found in Zn1Mg0.2Zr and Zn1Mg0.1Zr, respectively, as opposed to 0.070 mm per year in Zn1Mg alloy [22]. In comparison to other alloying elements, the addition of the proper amount of Sr aids in the induction of good quality mineralized bone in Mg-Zr alloys [43].

2.6.2 Influence of zinc

Zinc is one of the vital elements required in the human body for more than 300 enzymatic reactions, metabolism, and the transmission of genetic information. For Mg-based bone implants, zinc is preferred as an alloying element due to its biocompatibility, antibacterial ability, and osteogenic activity [44]. Zinc is added to magnesium-based implants to aid in grain refinement, and Mg-3 wt.% Zn dramatically reduced grain size, improving hardness, yield strength, ultimate strength, strain, and toughness [20]. Mg-3 wt.% Zn (MZ3) alloys fabricated using the hot rolling process can be used as bone implants. During hot rolling, grain size is refined due to deformation. In MZ3 alloys, corrosion increased initially due to mechano-chemical dissolution, but in the long run, the corrosion rate was decreased by the precipitation of a protective hydroxyapatite layer brought on by the formation of more nucleation sites in the grain boundary of fine-grained alloys. [20]. Figure 8 depicts the microstructure of Mg-Zn based biodegradable alloys, with different Zn contents.

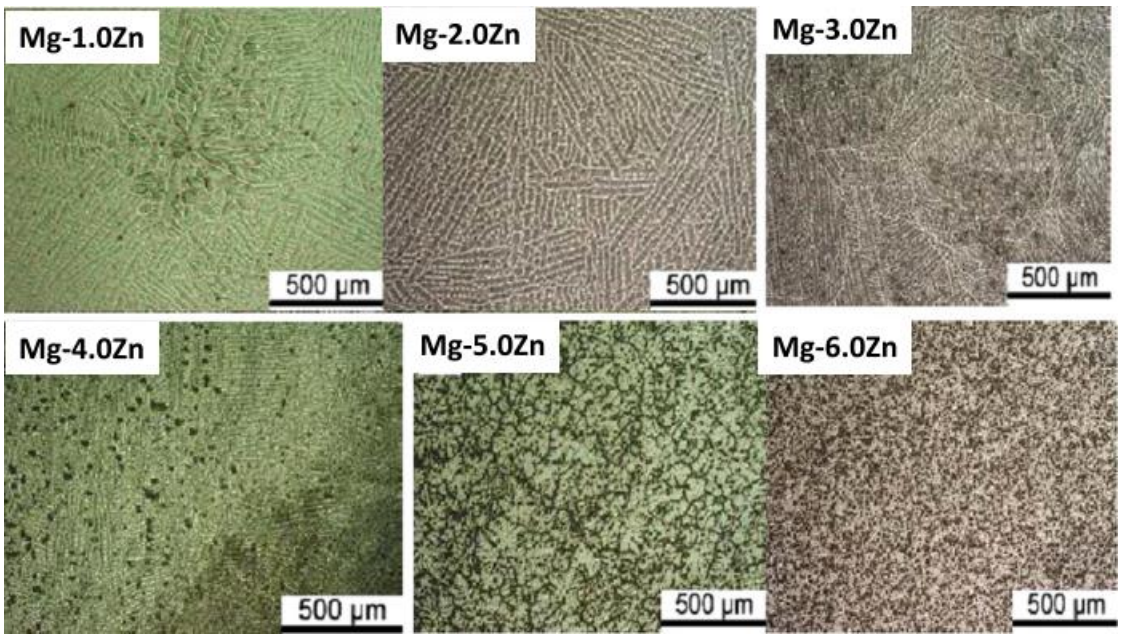

Figure 8: Microstructure of Mg-Zn alloys at various contents (wt.%) of Zn [45].

The ductility of implants and in vitro cell survival have been improved in the metallic alloys $Mg_{66}Zn_{30}Ca_4$ and $Mg_{70}Zn_{25}Ca_5$ [21]. If the amount of calcium is less than 1 wt.%, it also enhances the corrosion behaviour of a magnesium-based implant; however, if the amount is increased to 5 wt.%., there is a negative effect [21]. When zinc concentration was increased from 4 wt.% to 10 wt.% in alloys produced using selective laser melting, toughness increased, and no cracks were observed [46]. The biocompatibility of bone implants is enhanced by zinc. When 6 wt.% of zinc is added to a Mg-based implant, the rate of deterioration is 2.32 mm/year. When yttrium is combined with zinc, the solubility of zinc in the magnesium matrix is increased, improving mechanical properties, namely tensile strength, which aids in slowing the pace of degradation [18]. Furthermore, the mechanical characteristics of Zn are improved when combined with a non-toxic element like Mn up to 3 wt.%. Moreover, adding 1 wt.% of Mn together with Zn to the magnesium matrix has decreased the rate of corrosion. Additionally, Ca has a substantial impact on to what extent Mg-Zn alloys function mechanically and in terms of their ability to resist corrosion. For example, Mg-2Zn-0.24Ca alloys exhibit low corrosion rates even under

high torsional pressure because they contain a second nanoscale phase [18].

2.6.3. Influence of titanium

Titanium is one of the materials used in temporary bone implants because of its high strength-to-weight ratio and good biocompatibility. Mg-Ti based composite materials have emerged as biomaterials for bone implants because they combine titanium's high strength and corrosion resistance with magnesium's low elastic modulus and biodegradability, resulting in a biomaterial with an elastic modulus like human bone. One of the best methods for creating Mg-Ti alloys is powder metallurgy. The strength and biocompatibility of Mg-Ti composites can be enhanced by powder metallurgy using a balanced combination of Ti and Mg particles [47]. Figure 9 shows change in elastic modulus of Ti-based biomaterials.

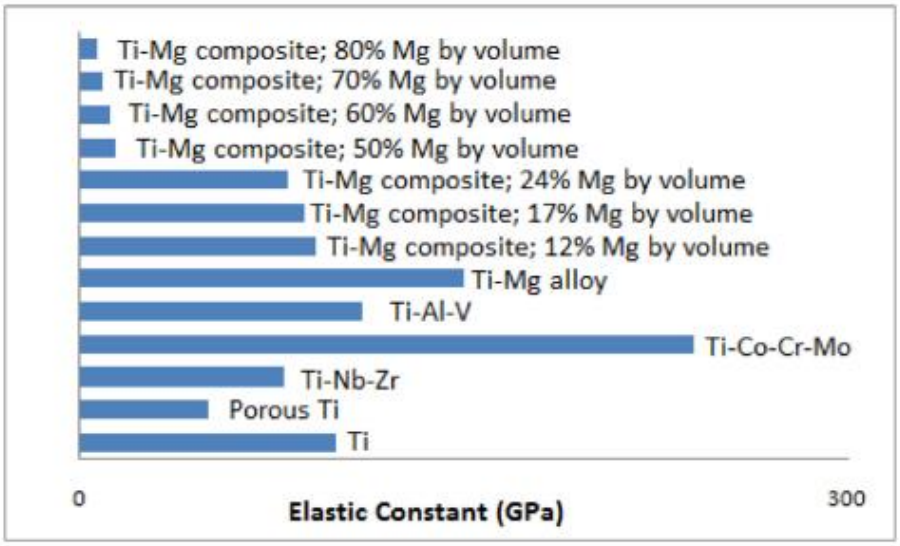

Figure 9: Elastic modulus of various Ti-based biomaterials [47].

When titanium content in Mg-Ti alloys is less than 40 wt.%, it does not have a significant effect on the elastic modulus of the alloy; hence, the Young´s modulus of Mg can be retained in the alloy, making its elastic modulus similar to that of bone. Mg alloy with a titanium content of 20 at. % prepared using a high-energy ball milling process shows a reduction in corrosion when tested in Hank´s solution at 37ºC. Using a high-energy ball milling process, the solid solubility of titanium in magnesium can be increased more than that foreseen at equilibrium [48].

2.6.4. Influence of calcium

Calcium is the most important element for human bones, which has a low density of 1.55 g/cm^3 and exists in the form of hydroxyapatite. Mg-Ca alloys have a similar density to human bone, which is beneficial for bone implants. Ca acts as a grain refiner when alloyed with Mg, where grain size reaches a stable level when the content of Ca in the Mg-Ca alloy is 0.5 wt.% [40]. Harandi et al. investigated the effect of Ca on the microstructure of Mg-Ca alloys, finding that increases in calcium content resulted in microstructure refinement and increased volume of the Mg_2Ca intermetallic phase in the Mg matrix along grain boundaries, increasing the alloy's hardness. The pH of plasma SBF is raised by the addition of calcium (3–4 wt.%), which has the effect of accelerating the development of

bone-like, needle-shaped apatite. However, the Mg_2Ca phase in the Mg-Ca alloy degraded at a rapid rate in response to increased calcium content. Mg-0.7 wt.% Ca is the optimum composition of Mg-Ca alloys which can be used as biodegradable bone implants [49].

Li et al. investigated Mg-xCa (x=1-3 wt.%) alloys and their potential use as biodegradable bone implants. Mg-1Ca implants possess biocompatibility and biodegradability. When the content of Ca in Mg-1Ca alloys is increased, the yield strength, UTS, and elongation of Mg-based alloys decrease. However, elongation and UTS were greatly enhanced by hot rolling and hot extrusion. After 90 days, radiographic results revealed that the pin of Mg-1Ca alloys had gradually degraded, and bone regeneration occurred after 3 months [50]. Figure 10 shows formation of α-Mg and Mg_2Ca eutectic along grain boundaries in Mg-3 wt.% Ca alloy.

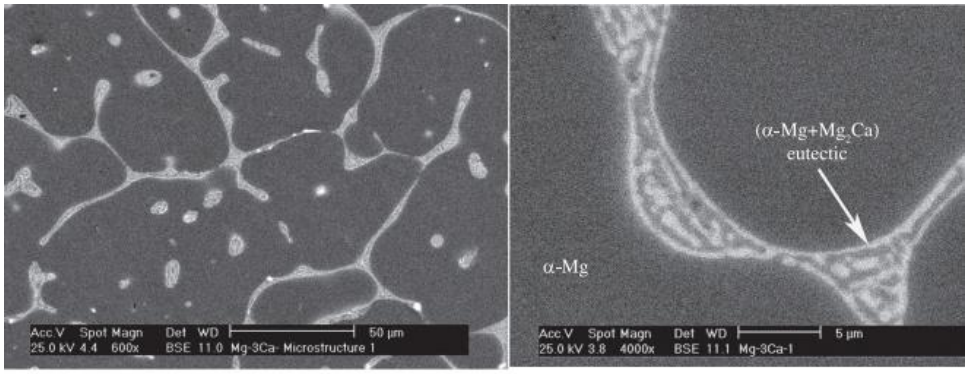

Figure 10: SEM image of Mg-3Ca alloy showing formation of α-Mg and Mg_2Ca eutectic [49].

Mg-0.3 at. % Ca biodegradable alloy fabricated by extrusion process possesses ultra-high grain refinement up to 0.5 µm and high tensile strength up to 400 MPa. This alloy can be used for bone fixation [51]. Rong Chang Zeng et al. studied the in vitro corrosion behaviour of an as-extruded Mg-xCa (x = 0.54, 0.79, and 1.35 wt.%) alloy. In comparison to Mg-0.54 wt% Ca and Mg-1.35 wt% Ca, Mg-0.79 wt% Ca alloy has the highest hardness, UTS, and yield strength, making it the best material for biomedical implants. These properties are due to its homogeneous microstructure. Pitting corrosion was observed to begin in α-Mg matrix near $Mg_2CaFeSi$ particles [52].

2.6.5. Influence of rare-earth elements

Rare-earth elements (REE) include seventeen elements, of which fifteen are lanthanides and two are scandium (Sc) and yttrium (Y). When combined with magnesium, REE improve the strength, hardness, and corrosion resistance of Mg-based alloys through solid solution and precipitation hardening. They are divided into two categories: those with high and those with low solubility [38]. Due to the formation of intermetallic phases like Mg_5Gd, gadolinium has the highest solubility in Mg, with 23.49 wt.%, comparable to dysprosium (Dy), which has 25.3 wt.%. By increasing the concentration of Gd up to 10 wt.%, corrosion resistance behaviour of Mg-based alloys is greatly improved. Additionally, adding Y increases corrosion resistance by producing yttrium oxides on the surface; 4 wt.% Y demonstrated the highest performance in terms of mechanical and corrosion properties [44].

Willbold et al. investigated the corrosion resistance behaviour of three binary REE (Lanthanum, Cerium, and Neodymium) alloys based on Mg: Mg-0.69wt%La, Mg-1.27wt%Ce, and Mg-2.13wt%Nd. $Mg_{12}Ce$, $Mg_{17}La$, and $Mg_{12}Nd$ intermetallic phases were identified, according to XRD data. Mg-La, Mg-Nd, and Mg-Ce all had corrosion rates of 1.35 mm/year, 0.91 mm/year, and 1.46 mm/year, respectively [53]. Figure 11 depicts microstructure of Mg-REE alloys where bright phases correspond to intermetallic precipitates which are rich in REE. When processing methods such as heat treatment, vacuum melting, and extrusion were used for casting ingots, the mechanical and corrosion behaviour of Mg-Y-Zr-based WE43 alloys improved significantly. This results from the strengthening of solid-solution and fine-grain boundaries. These processing methods minimized the corrosion rate of the alloys by converting severe diffusional corrosion into uniform corrosion [54].

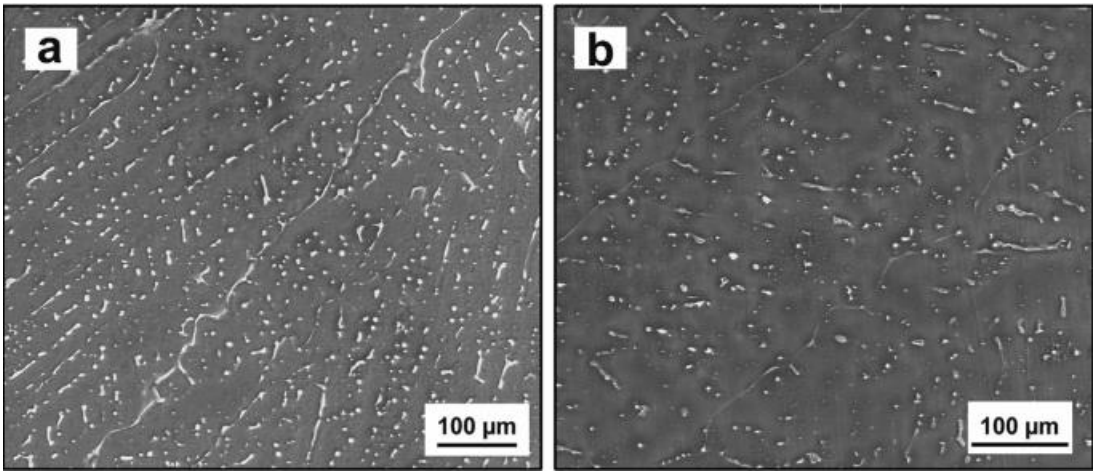

Figure 11: Microstructure of a) Mg-Ce; and b) Mg-La [53].

2.7. Mg-based coatings by DC magnetron sputtering

Sputtering was first employed for commercial purposes in coating procedures using diode sputtering in 1940, despite being discovered in 1850. After being "attacked" by extremely powerful ions, atoms are ejected from a target material through the process of sputtering. The low deposition rate and expensive cost of diode sputtering were two of its main disadvantages. Since 1970, magnetron sputtering has been utilized to speed up deposition and improve the collision of inert gas for ionization. With this method, a wide variety of metals and compounds can be deposited in a high vacuum environment. Some advantages of this approach include high deposition rates, adhesion, consistency in deposition, and excellent surface coverage. To attract positive ions for surface collision, a negative voltage (~-300 V) is applied to the target. Sputtering takes place when kinetic energy is transferred three times as much as the binding energy of the atoms on the surface, in a direction normal to the surface [55]. For the sputtering process, usually DC power sources are utilized for metals, whereas RF power and pulsed DC sources are employed for semiconductors and insulators [55]. Sputtering allows uniform coatings to be produced, which is not achievable with other techniques, making it an advantage of magnetron sputtering over more traditional techniques like melt spinning and copper mould injection-casting [27]. In addition, the solubility of the alloyed elements is higher in this technique compared to other traditional methods like casting and rolling. The high cooling rates in the sputtering process gives rise to metastable structures, which means that the solubility of Mg-based alloys can be increased.

The coatings deposited using magnetron sputtering allow for two-step corrosion behaviour, with the coating dissolving totally or partially during the second phase as the fracture heals [27]. The first phase of corrosion behaviour must have a low degradation rate to sustain fractured bone. In the work of Schluter et al. [27], Mg-Zn-Ca coatings with different chemical compositions were obtained, by adjusting the power applied to the target and the chamber pressure. The deposition parameters can be varied influencing the composition of the coatings. The sputtering chamber is kept at a base pressure of 1.4×10^{-3} Pa for the deposition of magnesium with zinc from 0 to 10 wt.%, and then argon ions are used for etching the substrates using a bias voltage of -600V for 20 minutes with an argon pressure of 0.8 Pa. After cleaning the substrates, a 2-micron coating is deposited using a pulsed DC power source with a power density of 1.3 W/cm^2 and a frequency of 20 kHz. The target's distance from the substrate is 90 mm [56]. Figure 12 shows a schematic representation of magnetron sputtering process.

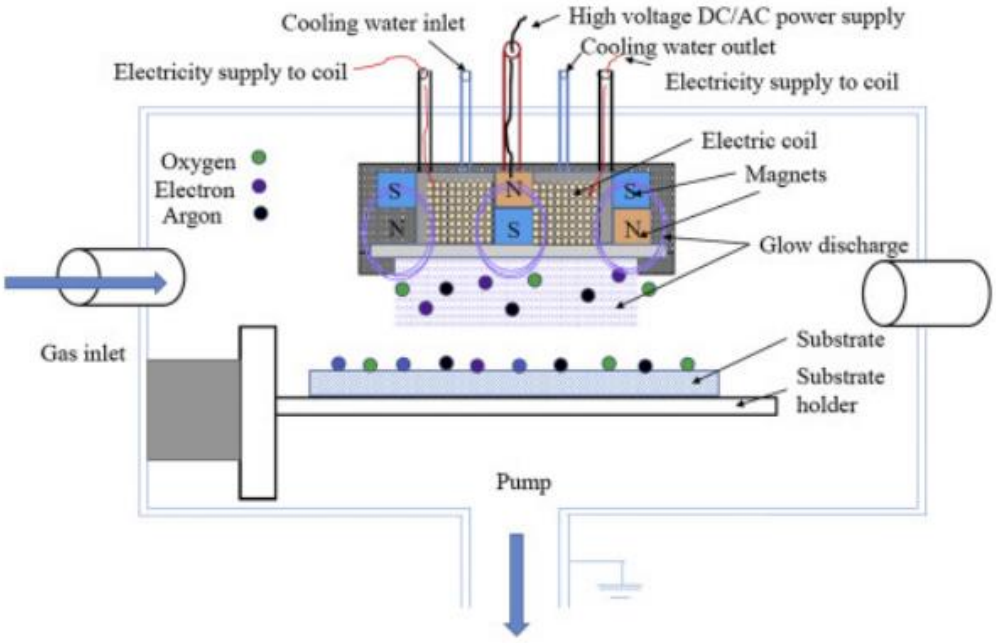

Figure 12: Schematic diagram of magnetron sputtering process [55].

3. Experimental Procedure

In this section, the techniques and conditions used to achieve the objective of the work are described. Initially, silicon wafers (100) and 316L stainless steel (SS) substrates with dimensions of 20×20 mm² were chosen as the substrates for the deposition of the Mg-(Zr) coatings. The silicon substrates were utilized for most characterizations, while corrosion and tribology tests employed the coated SS 316L substrates. To prepare the substrates, the surface of the SS 316L substrate was subjected to polishing using silicon carbide papers of varying grit sizes (240, 320, 600, 800, 1200, and 2500). This process was followed by the application of diamond suspension until a highly reflective, mirror-like finish was achieved. The silicon wafers were cut into 20×20 mm² dimensions to match the size of the SS substrates and fit into the substrate holder. Prior to deposition, the substrates were subjected to cleaning using acetone and ethanol in an ultrasonic bath for 10 minutes, and then fixed to the substrate holder before entering the sputtering chamber. Additionally, for later determination of film thickness via 3D profilometry, a drop of boron nitride was placed on one of the silicon substrates. All substrates were fixed to the substrate holder using silver paint. Various characterization techniques were employed to analyse the Mg-Zr coatings deposited using DC magnetron sputtering. These techniques included SEM (Scanning Electron Microscope), EDS (Energy Dispersive X-ray Spectroscopy), XRD (X-ray Diffraction), AFM (Atomic Force Microscope), and contact angle measurements to assess the film's morphology, chemical composition, crystal structure, surface topography, and wettability. Nanoindentation was used to determine mechanical properties such as hardness and Young's modulus of the coatings. The corrosion resistance behaviour of the deposited coatings was evaluated through EIS (Electrochemical Impedance Spectroscopy) and PP (Potentiodynamic Polarization) tests. Finally, the tribological behaviour of the coatings was assessed under dry conditions using a reciprocating tribometer. The subsequent sub-sections will provide some details of the various parameters involved in these procedures.

3.1. Development of Mg-Zr coatings by DC magnetron sputtering

Initially, the deposition of a pure magnesium coating onto Si and SS substrates was performed by magnetron sputtering in the HARTEC semi-industrial sputtering machine at CEMMPRE (Centre for Mechanical Engineering, Materials and Processes). The target material utilized in this process was pure magnesium. Afterwards, two targets were employed: magnesium (99.9% purity) and zirconium (99% purity), both with an area of 150×150 mm², to introduce zirconium into magnesium-based coatings. The zirconium content, ranging from 0 to 5 atomic percent, was controlled by adjusting the power density applied to the targets.

Before conducting the final depositions, a preliminary test was conducted on Si substrates using only the magnesium target. In this experiment, the zirconium target was covered, and the deposition chamber was allowed to reach a vacuum pressure of 9.6×10^{-4} Pa. Subsequently, etching was performed using argon gas at a pressure of approximately 0.2 Pa and a pulsed DC supply of -250V for 20 minutes was used to clean the substrates. Following etching, deposition started at a pressure of 3.5×10^{-1} Pa, with 500 W of power supplied to the magnesium target for 15 minutes under a bias voltage of -70V. The resulting film had a thickness of 1.8 µm, as measured by a profilometer.
For subsequent depositions, the power applied to the magnesium target remained constant until Mg-3.4Zr deposition. The power applied to the zirconium target was varied, starting

at 170 W for the Mg-5.0Zr film and reducing to 100 W for the remaining depositions (minimum power required to have plasma). To reduce the Zr content, the power supplied to the magnesium target was increased from 500 W to 730 W for Mg-2.0Zr. This value was further increased to 1500 W for Mg-1.0Zr. For the final deposition of Mg-0.4Zr, the zirconium target was partially covered by a shutter, while the power applied to the magnesium and zirconium targets remained at 1500 and 100 W, respectively. The DC power source used was a Huttinger PFG 7500 DC. The distance between the magnesium target and the substrates was 75 mm, while the distance between the zirconium target and the substrate was 95 mm. The substrate holder rotation speed was set at 23 rpm. Detailed parameters for the deposition of Mg-(Zr) coatings are provided in Table 1. Figures 13a and 13b illustrate the sputtering chamber and the HARTEC sputtering machine at CEMMPRE, respectively.

Table 1: Parameters for the deposition of Mg-Zr coatings.

Coatings	**Base pressure (Pa) ($\times10^{-4}$)**	**Deposition pressure (Pa) ($\times10^{-1}$)**	**Target 1(Mg) Power density (W/mm^2)**	**Target 2(Zr) Power density (W/mm^2)**	**Deposition time (min)**
Mg-0.0Zr	8.4	3.5	2.2×10^{-2}		18
Mg-0.4Zr	5.9	3.5	6.7×10^{-2}	4.4×10^{-3}	7
Mg-1.0Zr	5.9	3.5	6.7×10^{-2}	4.4×10^{-3}	7
Mg-2.0Zr	5.5	3.5	3.2×10^{-2}	4.4×10^{-3}	12
Mg-3.4Zr	4.5	3.5	2.2×10^{-2}	4.4×10^{-3}	18
Mg-5.0Zr	6.2	3.5	2.2×10^{-2}	7.6×10^{-3}	17.5

Note: All chemical compositions are in atomic percentage.

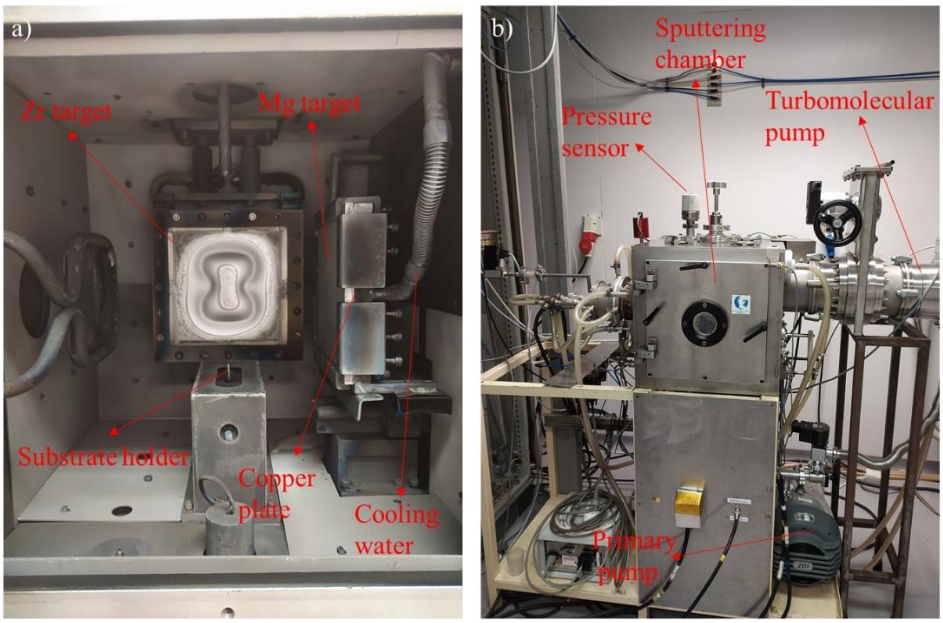

Figure 13: HARTEC sputtering equipment: a) sputtering chamber; and b) sputtering machine.

3.2. Morphological, chemical, and structural characterization

3.2.1. SEM and EDS

The morphology and chemical composition of all the deposited films were analysed using a Zeiss -Merlin field-emission SEM equipped with EDS. Top views of the morphological analysis were conducted using an accelerating voltage of 2 kV and a working distance of 6.2 mm, while cross-sectional views were obtained using a working distance of 5.6 mm. The analysis of the corroded Mg-Zr coatings was carried out using a Hitachi SU3800 SEM equipped with EDS at CEMMPRE with accelerating voltage of 10 kV.

3.2.2. XRD

GIXRD (Grazing Incidence X-ray Diffraction) was employed to characterize the structure of the Mg-Zr coatings. This technique allows the indexation of the crystalline phases present in the coatings. Crystallite size and crystal defects, namely dislocations' density, can be obtained. The Rigaku Smartlab X-ray diffractometer at IPN was utilized for the experiments, with CoKα radiation (wavelength of 1.789 Å) and a step-scan mode from 35º to 90º. The step size was 0.025º, and the sampling time was 1s per step. The peak position and FWHM were obtained using a pseudo-Voigt function. Bragg's law was applied to calculate the interplanar distance of atoms in the crystal, as well as the lattice parameters. The crystallite size was determined using the Scherrer equation [57], [58]:

$$D = \frac{K\lambda}{\beta cos\theta}$$

Where, K=dimensionless shape factor (0.9)
λ = wavelength of X-ray (1.789 Å)
β=FWHM in radian
θ=Bragg's angle

3.2.3 AFM

The surface topography of the Mg-Zr coatings was assessed using an AFM, specifically the Bruker Innova instrument located at CEMMPRE. The characterization was performed in tapping mode, whereby a cantilever with a SiN tip having a tip radius of less than 10 nm was employed. The experimental areas analysed had 5x5 μm². The objective of these experiments was to determine the surface roughness and porosity of the coatings under study. The obtained images were processed using Gwyddion software to extract various parameters, including roughness, skewness, and kurtosis.

3.2.4. Wettability

A wettability test was conducted to determine the surfaces' free energy and contact angles between the coated surfaces and various testing liquids. Evaluation of surface topography, including roughness and wettability, is crucial for implantable biomaterials as these factors significantly influence cell adhesion, cell proliferation, osteointegration, and implant durability [59]. Several liquids, such as plasma SBF, α-BNF, DM, ultrapure water (99.9%), and EG, were used in these studies. The experiments were performed using a Data Physics OCA20 instrument located at IPN which is shown in figure 14. Each liquid was tested on different samples three times throughout the experiments. A drop of the test liquid with a volume of 10 μL was injected from a syringe onto the surface of the coatings and allowed to remain for 60 seconds. The surface free energy was derived from the contact angles using the Owens-Wendt-Rabel-Kaeble (OWRK) model [60].

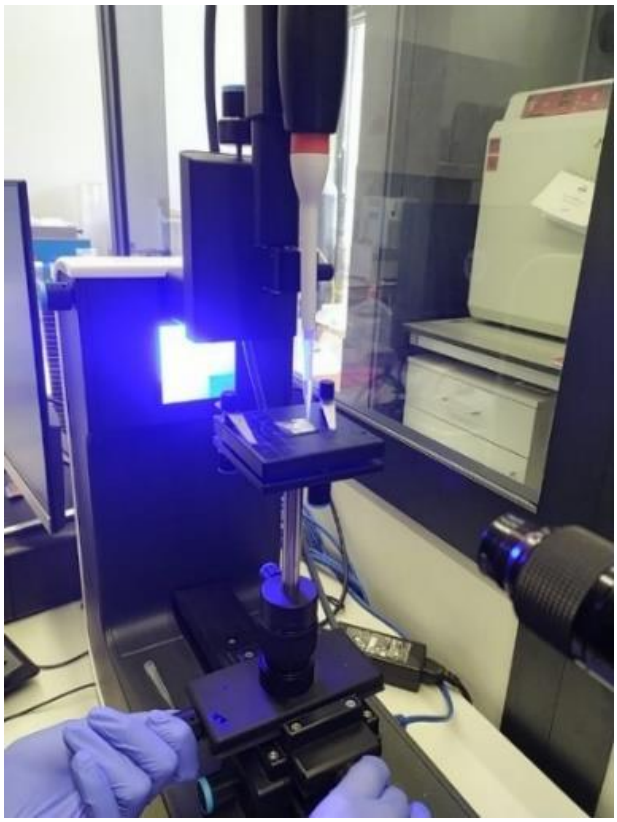

Figure 14: Wettability test on Mg-Zr coatings.

3.3. Mechanical characterization

Nanoindentation was conducted using a Micro Materials Nano Test instrument at CEMMPRE to evaluate the hardness and Young's modulus of the coatings. The nanoindenter is equipped with a Berkovich diamond pyramid indenter. A peak load of 1.5 mN was applied at a loading rate of 0.05 mN/s. The depths of indentation were kept below 10% of the coating thickness to avoid the influence of the substrate (SS 316L) on the experimental results. A Hardness and Young's modulus were determined using the Oliver and Pharr analysis method [61]. A minimum of 30 indentations were carried out per each coating. Fused quartz was used as a reference material to determine the Berkovich tip area function.

3.4. Corrosion test

In order to evaluate the corrosion resistance of the Mg-Zr coatings, corrosion tests were performed using EIS and PP techniques. These experiments were conducted at CEMMPRE within a Faraday cage to minimize external signal that could interfere with the electrochemical system of the corrosion setup. Plasma SBF was utilized as the electrolyte to simulate realistic environmental conditions similar to the human body.

The composition of the plasma SBF electrolyte used was as follows: sodium chloride (NaCl) (8.035 g), sodium hydrogen carbonate ($NaHCO_3$) (0.355 g), potassium chloride (KCl) (0.225 g), di-potassium hydrogen phosphate trihydrate ($K_2HPO_4 \cdot 3H_2O$) (0.231g), magnesium chloride hexahydrate ($MgCl_2 \cdot 6H_2O$) (0.311 g), 1.0 M hydrochloric acid

(HCl) (39 ml), calcium chloride ($CaCl_2$) (0.292g), sodium sulphate (Na_2SO_4) (0.072 g), Tris-hydroxymethyl aminomethane ($(HOCH_2)3CNH_2$) (Tris) (6.118 g), and 1M hydrochloric acid (5 ml) [62]. The experiments were conducted at a temperature of 37ºC, which closely resembles the temperature of the human body. A thermostat was used to heat a water bath circulating around the cell, ensuring a stable temperature. The cell employed in the experiments consisted of three electrodes: a saturated calomel electrode with KCl as the reference electrode, platinum (Pt) as the counter electrode, and the coatings as the working electrode. All the experiments were performed using a Gamry 600 potentiostat, with three experiments conducted for each chemical composition in both EIS and PP measurements. Figure 15 illustrates the setup utilized for the corrosion tests.

Initially, preliminary EIS tests were conducted for 24 hours and 48 hours to determine the time for complete degradation of the coatings. However, the coatings were fully corroded after 24 hours, and hence the following experiments were conducted only during the time required to stabilize the open circuit potential (OCP). In these experiments, the coatings were mounted in the cell, and then plasma SBF was poured into it. Afterwards, the thermostat was set at 47ºC to obtain 37ºC in the electrolyte, and it took nearly 45 minutes to reach a stable temperature. As soon as the temperature was reached, electrodes were connected to the cell, and the EIS experiment was started. EIS measurements were done after stabilization of OCP (~300 seconds). In this experiment, 8 points per decade were taken with a 10 mV/s scan rate and a frequency range from 0.1 Hz to 100 kHz.

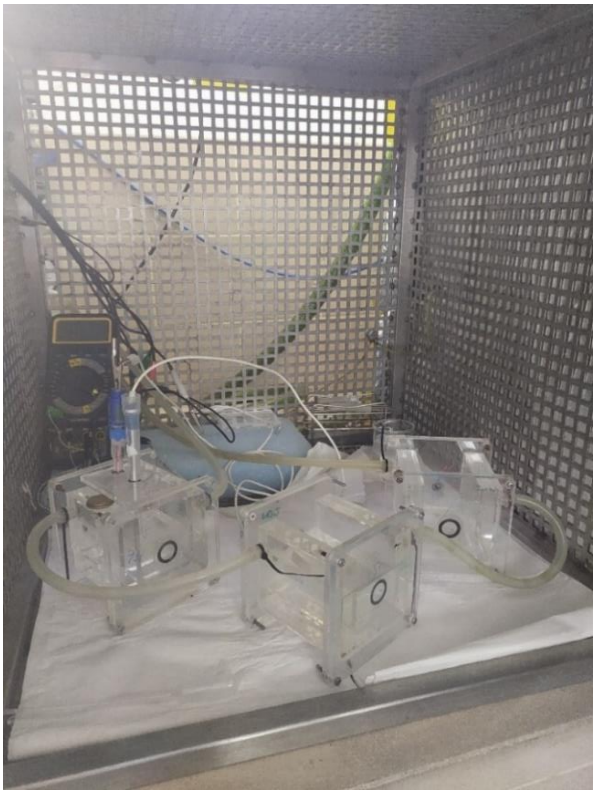

Figure 15: Corrosion test set up used for measurement of EIS and PP inside Faraday cage.

Similarly, to conduct the PP tests, -200 mV and +200 mV vs. E_{OCP} were used with a scan rate of 0.15 mV/s. The measurements were performed after stabilization of the temperature at the cell (37ºC), similar to the EIS conditions. The obtained data was fitted using Gamry Echem software. The equivalent weight of the coatings was obtained from EDS measurements and later, it was employed to calculate the corrosion rates based on the ASTM G102-89 standard [63].

3.5. Tribological characterization

The tribological characterization of the Mg-Zr coatings was conducted using a Rtec equipment, specifically the reciprocating tribometer of IPN which is shown in figure 16. The tests were performed under dry conditions, with a stroke length of 4 mm, a frequency of 1 Hz, and a load of 2 N, for 1 minute using ball-on-flat sliding wear method, to simulate the micromovements of a bone implant within the human body [64]. Initially, a 10-minute test was conducted under dry conditions, but the coatings failed, resulting in a penetration up to a depth of 6 to 8 µm, which exceeded the thickness of the coatings (close to 2 µm). Consequently, the testing time was reduced to 1 minute, during which the wear track depth was approximately 2 µm, enabling the determination of the coatings' wear rate. The counter body used for the test was an alumina ball with a diameter of 9.5 mm. The experimental procedure was conducted three times for each coating under ambient temperature and atmospheric pressure. The results for COF (Coefficient of Friction) and specific wear rates were obtained by calculating the average of the three tests. Specific wear rates were calculated using ASTM G133-05 [65]. Specifically, for the tribological characterization, only the Mg-Zr coatings with the best corrosion resistance in a plasma SBF environment were selected. Pure magnesium and the substrate were chosen as reference materials for comparison.

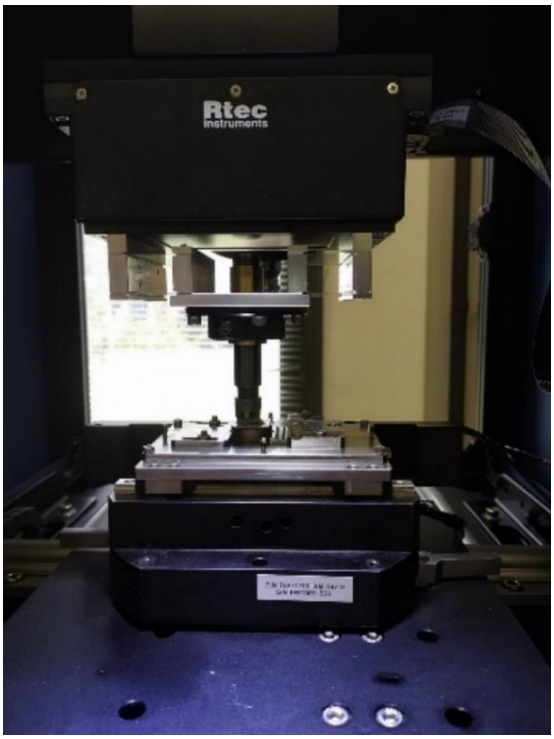

Figure 16: Reciprocating tribometer set up for tribological tests of the Mg-Zr coatings.

4. Results and Discussion

In this section, the results obtained for Mg-Zr coatings with different chemical compositions are analysed, and these results are correlated with the doping effect of Zr in pure Mg coatings. Morphological, chemical, structural, mechanical, and surface properties are correlated with the corrosion behaviour of the coatings. In the case of corrosion results interpretations, SS 316L was used as a reference, which was the substrate material used in this work.

4.1 Morphological, chemical, structural, and topographical characterization

4.1.1. Morphology and chemical composition

The Zr content was varied by adjusting the power applied to each target. Table 2 provides power density of two targets ,the thickness and deposition rate of the coatings, accompanied by the respective chemical composition. The deposition rate was determined by considering the deposition time and the coatings' thickness. It can be noted that, as expected, with the increase of the power density applied to the Mg target (Mg-1.0Zr and Mg-0.4Zr) there was an increase in the deposition rate. The primary objective was to investigate the properties of coatings with similar thickness (~2 µm) for comparing their corrosion and tribological behaviour. Figure 17 exhibits EDS scans of the pure Mg coating as well as of the coating with the highest Zr content.

Table 2: Power density, thickness, and deposition rate of the Mg-Zr coatings.

Coatings	**Power density (W/mm^2)**		**Deposition time(mins)**	**Thickness (µm)**	**Deposition Rate (µm/mins)**
	Target 1 (Mg)	**Target 2 (Zr)**			
Mg-0.0Zr	2.2×10^{-2}		18	2.2	0.12
Mg-0.4Zr	6.7×10^{-2}	4.4×10^{-3}	7	2.5	0.36
Mg-1.0Zr	6.7×10^{-2}	4.4×10^{-3}	7	2.7	0.39
Mg-2.0Zr	3.2×10^{-2}	4.4×10^{-3}	12	2.5	0.21
Mg-3.4Zr	2.2×10^{-2}	4.4×10^{-3}	18	2.4	0.13
Mg-5.0Zr	2.2×10^{-2}	7.6×10^{-3}	17.5	2.2	0.13

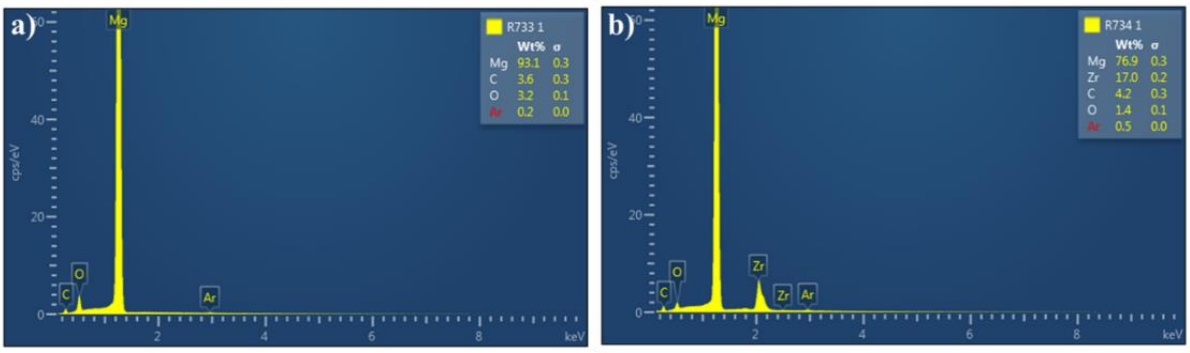

Figure 17: EDS scans of a) Mg-0.0Zr; and b) Mg-5.0Zr coatings.

In addition to Mg and Zr, the coatings contained impurities such as carbon (C), oxygen (O), and argon (Ar). The presence of these impurities was expected and common in most coatings developed using DCMS. To obtain the Zr contents (for comparative purposes), only Mg and Zr were quantified.

Figures 18 and 19 depict the morphology of the coatings, providing both top views and cross-sectional views of the coatings. Pure magnesium in figure 18a shows flake like structure. The top view shows distinct hexagonal shapes corresponding to the top of the columns for 18b,18c and 18d. As the content of Zr increases, the columnar boundaries become more refined, as demonstrated in figures 18e and 18f. This phenomenon corresponds to the grain refinement effect of Zr in the Mg matrix, as reported in literature [40].

Figure 19 exhibits a columnar growth pattern for all the Mg-Zr coatings, accompanied by the presence of some voids. In figures 19b, 19c, and 19d, the column width appears greater compared to the other coatings, which can be attributed to the higher deposition rate. This particular morphology, characterized by wider columns, aligns with zone 2 of the structure zone model proposed by Thronton [66].Conversely, figures 19e and 19f exhibit more compact coatings with slender columns and reduced voids. This can be attributed to a higher Zr content in the magnesium matrix and a lower deposition rate. The observed reduction in inter-column spacing and the presence of a more refined microstructure also aligned with zone 2 but closer to zone T of Thornton's model [67], [68].

During the deposition of a pure magnesium coating on a silicon substrate, Michael Stormer et al. [69] observed the development of columnar structures with voided boundaries, oriented parallel to the substrate's basal plane. These observations align with current work.

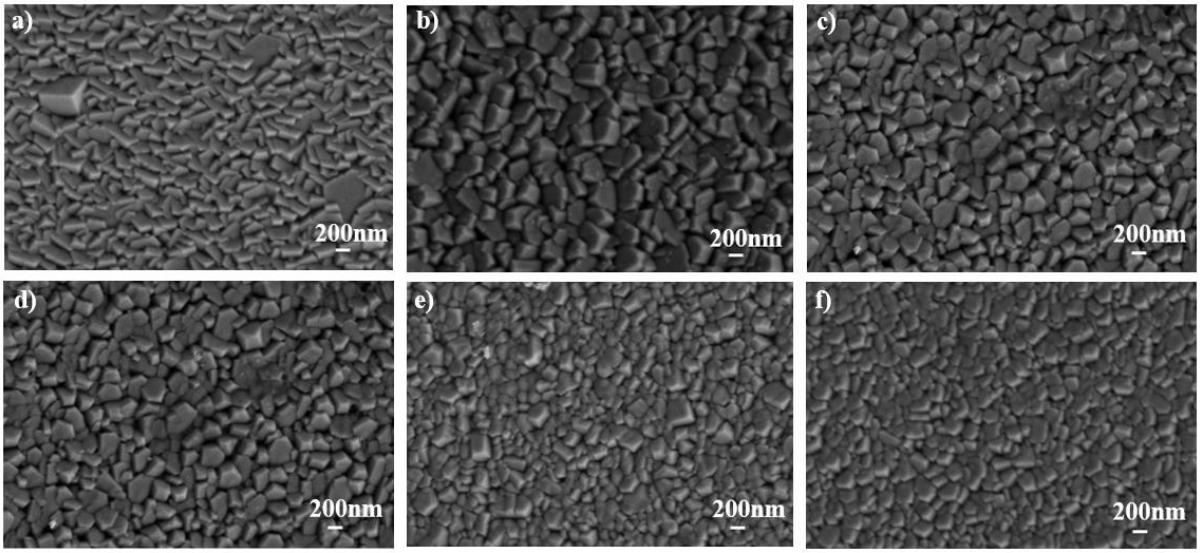

Figure 18: SEM top view images: a) Mg-0.0Zr; b) Mg-0.4Zr; c) Mg-1.0 Zr; d) Mg-2.0 Zr; e) Mg-3.4Zr; and f) Mg-5.0Zr.

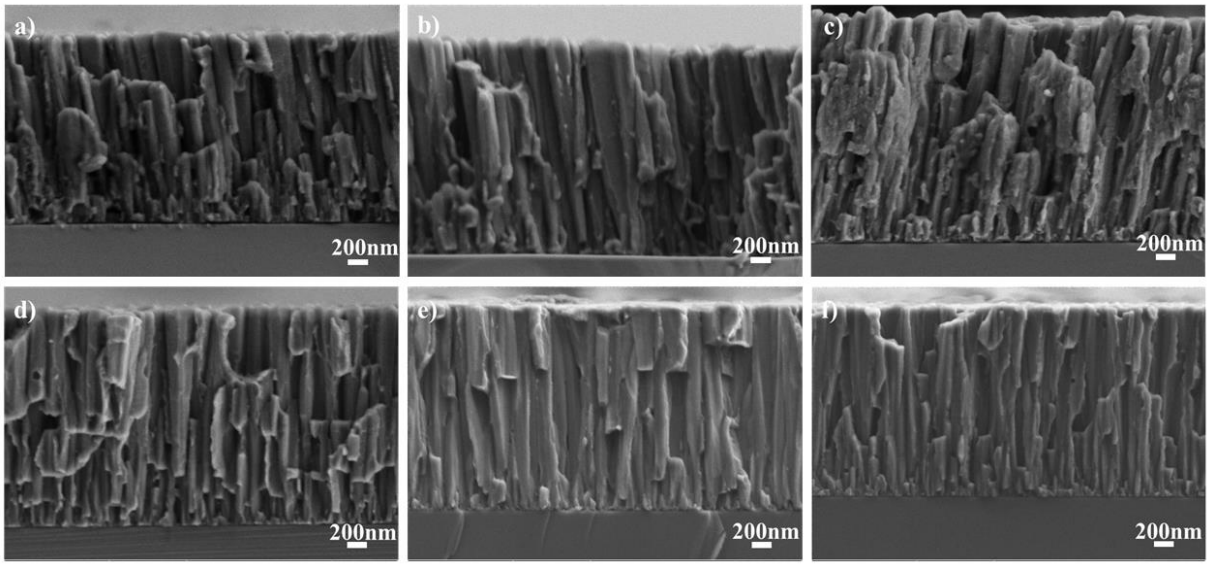

Figure 19: SEM cross-sectional images: a) Mg-0.0Zr; b) Mg-0.4Zr; c) Mg-1.0Zr; d) Mg-2.0Zr; e) Mg-3.4Zr; and f) Mg-5.0Zr.

4.1.2. Structure and crystallite size

The crystal structure of Mg-Zr coatings was investigated using Rigaku Smartlab grazing X-ray diffraction, allowing for the identification of various peaks in the XRD patterns. To identify these peaks, ICDD card no. 00-035-0821, corresponding to Mg, was utilized. All observed XRD peaks corresponded to the different planes of magnesium having HCP structure, namely (10.0), (00.2), (10.1), (10.2), (10.3), (20.0), and (20.1). In pure magnesium (Mg-0.0Zr) coatings, a preferential orientation along the (10.2) plane is observed, while for the coatings with Zr the (00.2) plane dominated, as shown in figure 20.

The XRD patterns demonstrate a clear rightward shift (higher angle) of peaks with increasing Zr content, particularly evident in the magnified view of the (00.2) peak displayed in figure 21. This shift can be attributed to changes in the lattice parameters "a" and "c" due to the doping effect of Zr in the Mg matrix. According to Table 3, an increase in Zr content led to an increase in lattice parameter “a” and decrease in the c/a ratio. This can be due to the overlapping of electrons at the first Brillouin zone in a perpendicular direction to the “c” axis. However, the opposite effect was found in the case of the lattice parameter “c”, as the value of the “c” parameter decreased with an increased Zr content. This can be explained by the relative atomic size of Zr, which is smaller than Mg in the lattice due to large interatomic forces resulting from the higher electronegativity of Zr [70]. No distinct peaks of Zr can be identified in the XRD patterns, despite the increase in Zr concentration up to 5.0 at.%. Similar lattice parameters (HCP and similar atomic size) might be the reason for this phenomenon. In fact, the positions of the XRD peaks in Zr (ICDD card 00-005-0665) are close to the ones in the Mg card.

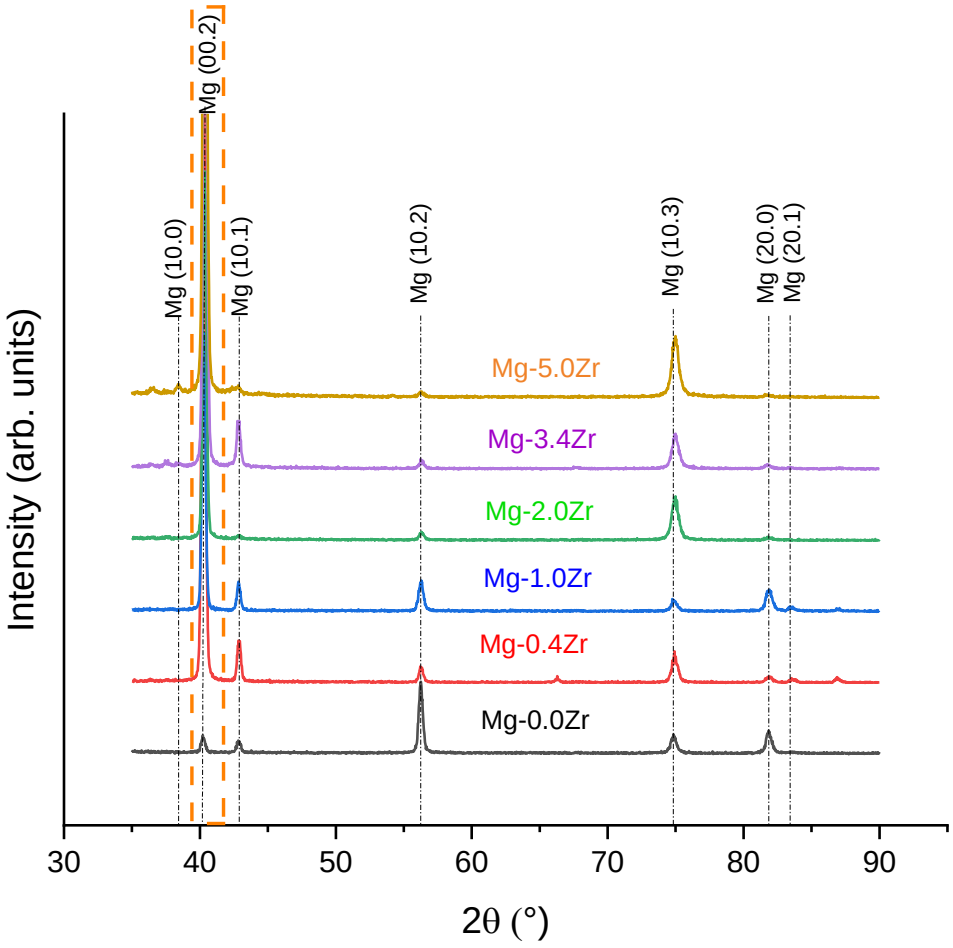

Figure 20: XRD diffractograms of Mg-Zr coatings with different Zr contents.

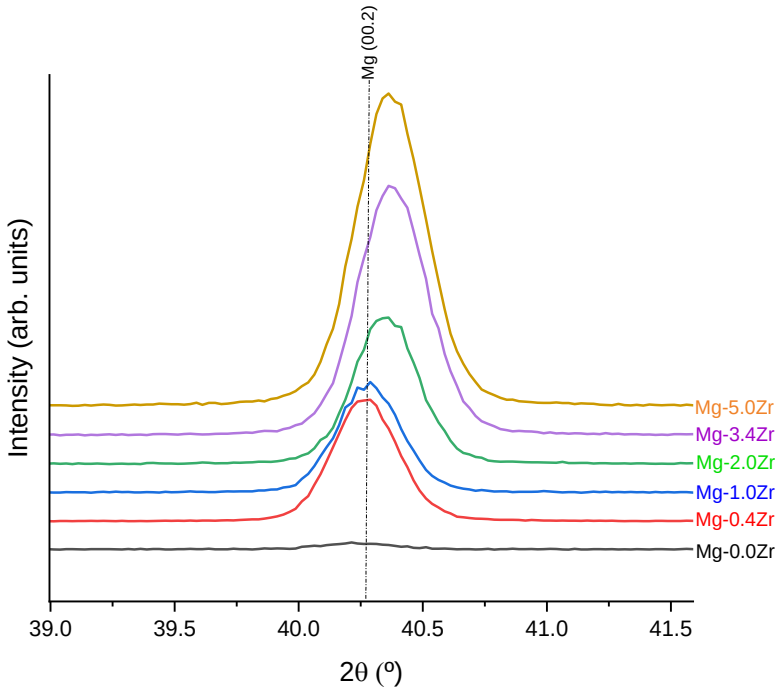

Figure 21: Magnified XRD diffractograms including Mg (00.2) plane.

Table 3: Lattice parameters of Mg obtained using (00.2) and (20.0) planes.

Coatings	Miller indices			Bragg's angle (°)	d-spacing(Å)	Lattice constant (Å)		c/a ratio
	h	k	l			a	c	
Mg-0.0Zr	0	0	2	40.24	2.6006		5.2013	1.6495
	2	0	0	81.86	1.3653	3.1532		
Mg-0.4Zr	0	0	2	40.27	2.5987		5.1973	1.6488
	2	0	0	81.89	1.3649	3.1521		
Mg-1.0Zr	0	0	2	40.28	2.5977		5.1954	1.6479
	2	0	0	81.88	1.3651	3.1526		
Mg-2.0Zr	0	0	2	40.35	2.5934		5.1869	1.6452
	2	0	0	81.87	1.3652	3.1527		
Mg-3.4Zr	0	0	2	40.38	2.5918		5.1837	1.6425
	2	0	0	81.77	1.3666	3.1559		
Mg-5.0Zr	0	0	2	40.37	2.5923		5.1847	1.6429
	2	0	0	81.78	1.3665	3.1557		

Note: standard value of "a" =3.2094 Å and "c" =5.2112 Å for HCP Mg

The introduction of Zr, with its smaller atomic size, into the crystal lattice of the coatings might have led to a decrease in the interplanar distance, resulting in the shifting of peaks

to higher angles. Figure 22 illustrates this phenomenon, displaying a decrease in the interplanar distance with an increase in Zr content. Moreover, the addition of Zr slightly reduced the crystallite size, which can be attributed to the grain-refining effect of Zr. Table 4 includes crystallite size of the Mg-Zr coatings obtained using Scherrer's equation.

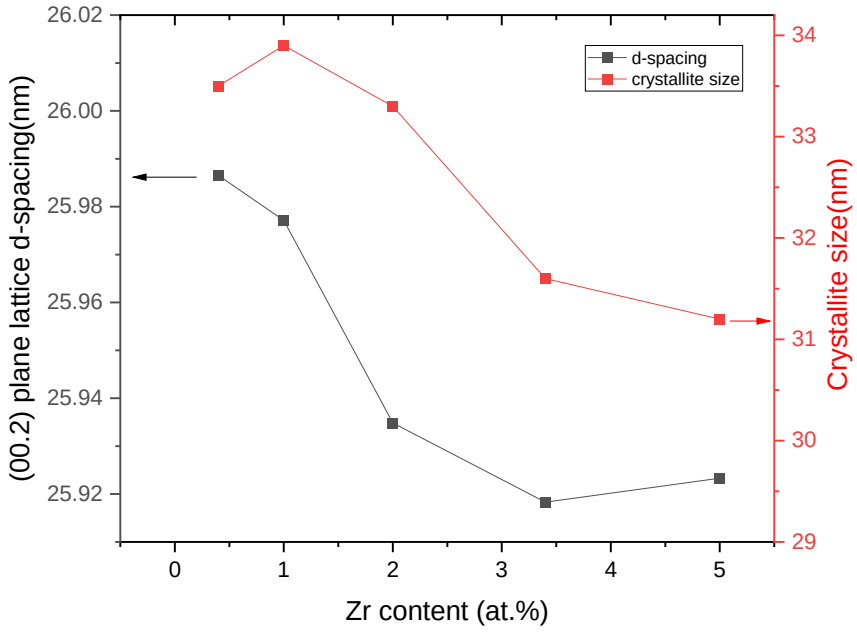

Figure 22: Interplanar distance and crystallite size after Zr addition into the Mg matrix.

Table 4: Crystallite size (D) of Mg-Zr coatings with increase in Zr content.

Coatings	Peak (hkl)	FWHM (°)	2Θ (°)	D (nm)
Mg-0.0Zr	(002)	0.35	40.24	29.60
	(102)	0.35	56.25	31.30
Mg-0.4Zr	(002)	0.31	40.29	33.50
Mg-1.0Zr	(002)	0.30	40.28	33.90
Mg-2.0Zr	(002)	0.31	40.35	33.30
Mg-3.4Zr	(002)	0.32	40.38	31.60
Mg-5.0Zr	(002)	0.33	40.37	31.20

4.1.3. Surface topography

The surface topography of Mg-Zr coatings was assessed using AFM images, as depicted in figure 23, which provided a 2D and 3D visualization of the coatings' surface. The roughness analysis was conducted over a measurement area of 5×5 μm^2, and various roughness parameters including mean roughness (S_a), root mean square roughness (S_q), skewness, and kurtosis were obtained and are presented in Table 5.

The findings indicate that increasing the Zr content initially led to an increase in roughness, followed by a subsequent decrease. The Mg-0.4Zr, Mg-1.0Zr, and Mg-2.0Zr

coatings, deposited applying higher power densities to the Mg target, exhibited higher roughness values in comparison to the other coatings. Notably, among these coatings, Mg-0.4Zr exhibited the highest roughness when compared to the remaining films, as indicated in Table 5. The surface roughness evolution matched SEM top view images. The AFM images illustrated that the films became more compact as the Zr content increased. It was noted that the surface topography of Mg-0.0Zr differed significantly from the other coatings, displaying a flake-like surface morphology. This observation was consistent with the SEM results. Furthermore, the Mg-2.0Zr coating displayed rougher surfaces with distinct deep valleys and fewer peaks, represented by the negative skewness value. A higher kurtosis value suggests sharper peaks, whereas a negative skewness value indicates the presence of deep valleys within the coatings [71].The increased roughness and the presence of deep valleys significantly impact the corrosion rate, as these factors indicates that the coatings are more susceptible to electrolyte attack, thereby promoting pitting corrosion. This aspect will be addressed in subchapter 4.3.

Table 5: Surface roughness parameters of Mg-Zr coatings.

Coatings	**Mean roughness S_a (nm)**	**Root mean square roughness S_q(nm)**	**Skewness**	**Kurtosis**
Mg-0.0Zr	17	22	-0.14	0.94
Mg-0.4Zr	29	34	-0.10	0.00
Mg-1.0Zr	21	26	-0.05	0.09
Mg-2.0Zr	22	27	-0.12	-0.30
Mg-3.4Zr	17	21	0.22	0.23
Mg-5.0Zr	13	16	0.24	0.23

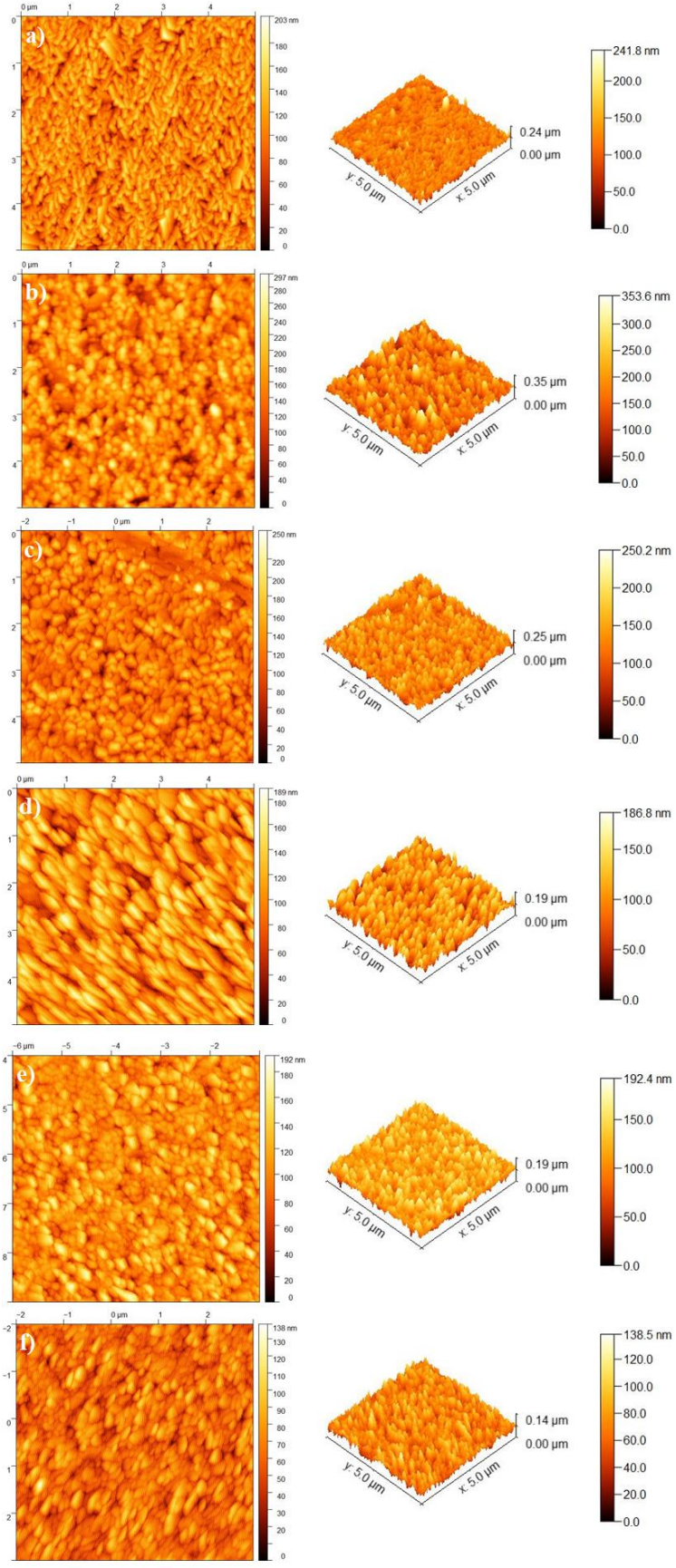

Figure 23: AFM images of Mg-Zr coatings: a) Mg-0.0Zr; b) Mg-0.4Zr; c) Mg-1.0 Zr; d) Mg-2.0Zr; e) Mg-3.4Zr; and f) Mg-5.0Zr.

4.1.4. Wettability

Measurements were conducted to determine the contact angle and surface free energy (SFE) of liquids on the Mg-Zr coatings. Five different liquids, namely α-bromonaphthalene, water, plasma SBF, ethylene glycol, and diiodomethane, were employed to assess the SFE of the coatings. The results of the contact angle measurements indicated that all the coatings exhibited a liquiphilic behaviour (contact angle < 90º).

The contact angle measurements for α-BNF ranged from 22º to 50º, indicating the oleophilic nature of the Mg-Zr coatings. Similarly, the contact angles for water ranged from 51º to 75º, revealing the hydrophilic behaviour of the coatings. The surface free energy was calculated using the OWRK (Owens-Wendt-Rabel-Kaelble) model [72] based on the contact angle measurements. Figure 24 represents the contact angle measurements performed using a Data Physics OCA20 instrument, while figure 25 provides a graphical representation of the contact angle values. Many researchers suggest that wettability and surface free energy are crucial for adhesion and bone matrix formation. Surface chemical characteristics determine surface free energy, which affects wettability and protein adsorption. Higher surface energy means better wettability and increased affinity for protein adsorption. Theoretically, it is expected that the high surface energy to enhance the osseointegration due to the larger protein adsorption. It also stimulates the activation of osteoblastic cells, contributing to bone integration [73] .

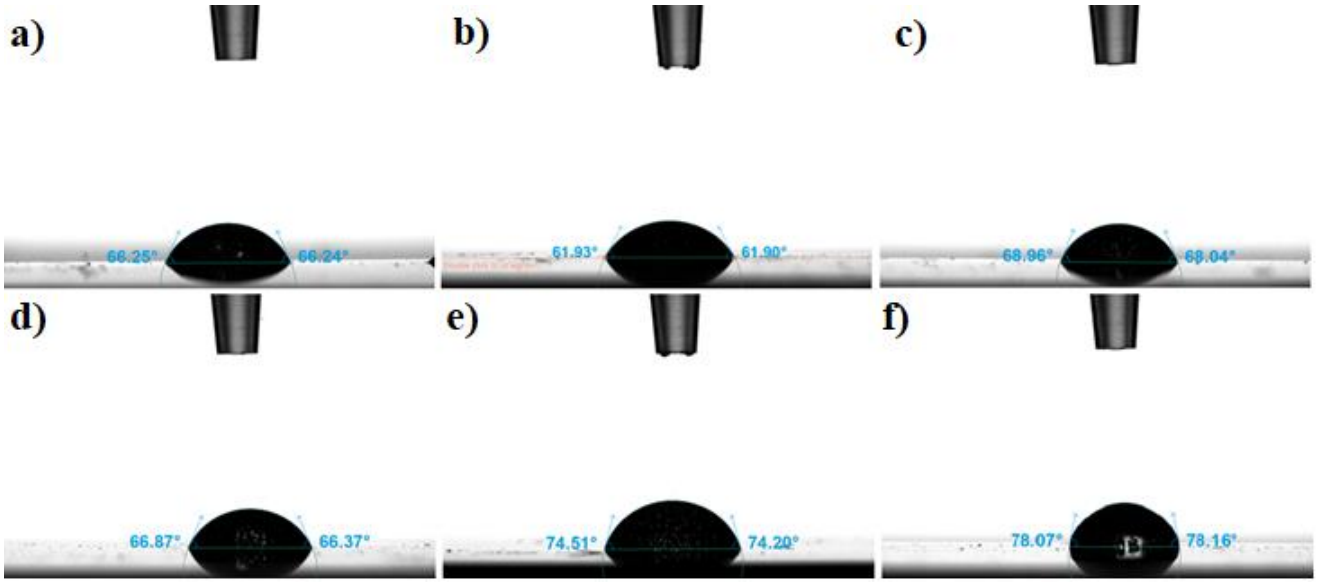

Figure 24: Contact angle images of all coatings: a) Mg-0.0Zr; b) Mg-0.4Zr; c) Mg-1.0Zr; d) Mg-2.0Zr; e) Mg-3.4Zr; and f) Mg-5.0Zr.

Table 6 presents the contact angle measurements conducted on the coatings under study using plasma SBF. Among the coatings, Mg-1.0Zr exhibited a higher SFE value of 48 mN/m, indicating good tissue compatibility [74]. However, Mg-5.0Zr showed a lower SFE value of 35 mN/m, with a minimum value of the polar component of SFE (5 mN/m). This suggests a decrease in bioactivity with an increasing Zr content in the Mg-Zr coatings.

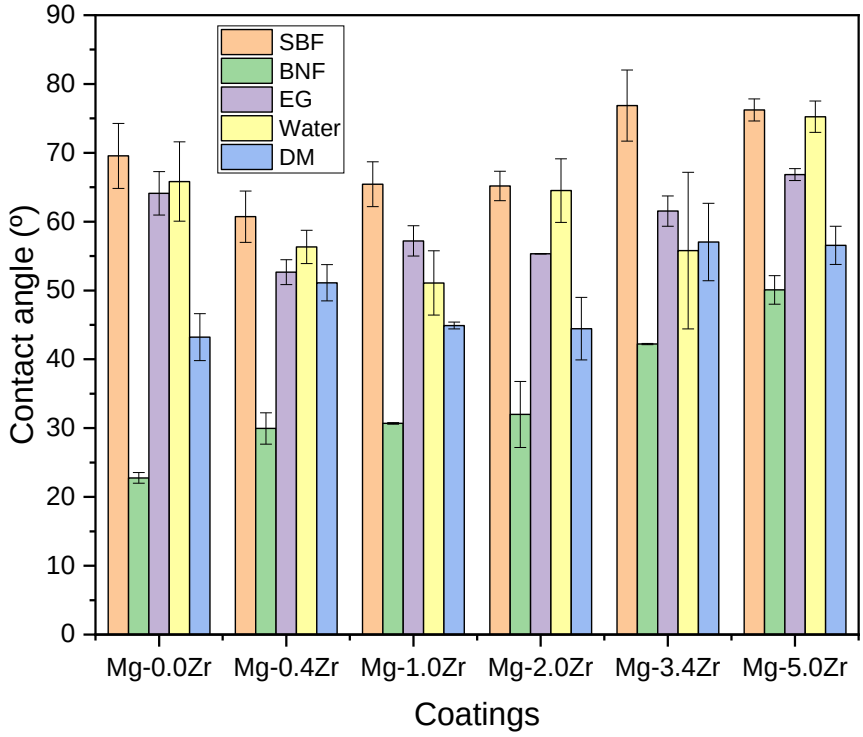

Figure 25: Contact angles for different liquids on Mg-Zr coatings' surface

Table 6: Contact angle and surface free energy of Mg-Zr coatings in plasma SBF.

Coatings	**SBF CA (°)**	**SFE (γ_p) (mN/m)**	**SFE(γ_d) (mN/m)**	**SFE (γ_{total}) (mN/m)**
Mg-0.0Zr	70±5	6	36	42
Mg-0.4Zr	61±4	12	34	46
Mg-1.0Zr	65±3	14	34	48
Mg-2.0Zr	65±2	9	35	44
Mg-3.4Zr	77±5	10	29	39
Mg-5.0Zr	76±2	5	30	35

4.2. Mechanical behaviour

Hardness and Young's modulus are critical parameters for evaluating the mechanical properties of coatings. Hardness refers to the resistance of a material to plastic deformation. Figure 26 illustrates the indentation marks performed on the Mg-2.0Zr coating, and detailed results of nanoindentation tests are provided in Table 7. Exemplificative loading/unloading curves of some tests are shown in figure 27. It is worth noting that with increase in Zr content, the penetration depth, and the plastic work (the surface area under loading/unloading curve) decreased. This indicated increase in hardening effect of Zr in the Mg matrix.

Figure 28 illustrates the hardness and Young's modulus evolution against Zr content. The

hardness of the coatings increased with higher Zr content. However, for Mg-0.4Zr and Mg-1.0Zr films, the hardness was even lower than that of Mg-0.0Zr coating. This discrepancy can be attributed to the coatings' morphology, which in turn is influenced by the deposition rate. In fact, higher deposition rates resulted in wider columns and in the presence of voids responsible for lower hardness values. Overall, the incorporation of Zr into the Mg matrix contributed to an increase in coatings' hardness.

S.Y. Kuan et al. [75] observed a similar trend in Mg-Cu-Zr films, where the hardness decreased significantly with increasing Mg content. During nanoindentation, non-basal slip mechanisms were easily activated under the 3D stress state, resulting in decreased hardness with higher Mg content.

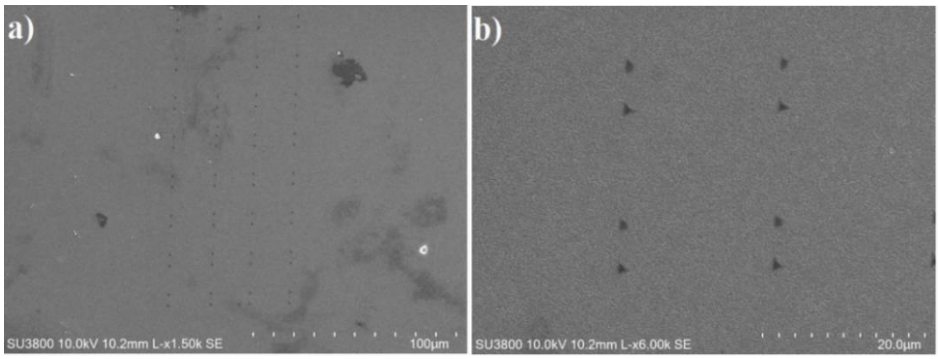

Figure 26: Example of nanoindentation marks done on the Mg-2.0Zr coating.

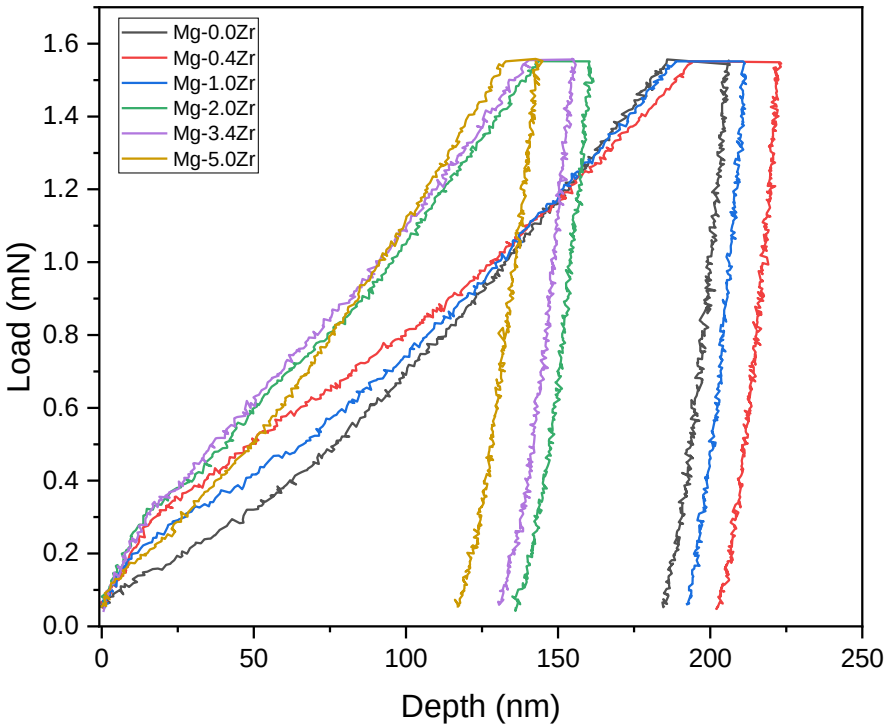

Figure 27: Example of loading/unloading curves for the various Mg-Zr coatings.

However, there was no significant differences in Young's modulus with increase in the amount of Zr. In fact, the coatings are mainly constituted by magnesium, therefore the Young's modulus that depends on the chemical bonding should not be influence by small Zr additions. Similar results had been reported S.Y. Kuan et al. [75] for Mg-Cu-Zr films. It is worth noting that although the measurements were performed using loads that give rise to indentation depths lower than 10% of the coatings' thickness (Table 7), regarding the Young's modulus the influence of the substrate cannot be ignored. Therefore, the Young's modulus of the coatings appears to be relatively high compared to the magnesium standard value of 40-55 GPa. The incorporation of Zr in the Mg host material may introduce lattice distortions and strain fields around Zr atoms. These distortions hinder the movement of dislocations leading to an increase in hardness.

The H/E ratio is an important factor for determining the mechanical behaviour of coatings, as higher H/E ratios indicate better resistance to plastic deformation and improved adhesion. In Table 7, Mg-0.4Zr and Mg-1.0Zr exhibited lower H/E ratios of 0.01 compared to other coatings, indicating their reduced resistance to plastic deformation. Mg-5.0Zr displayed a higher H/E ratio of 0.03, suggesting its better mechanical properties compared to the other coatings.

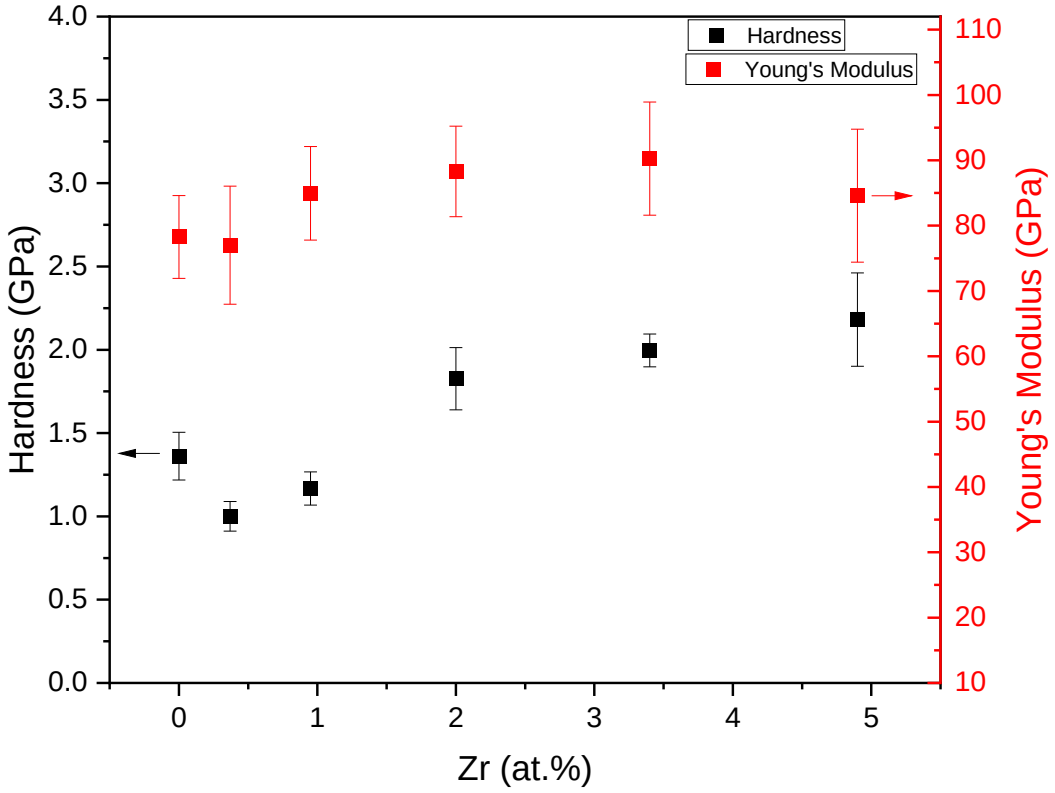

Figure 28: Hardness and Young's modulus of Mg-Zr coatings with different Zr contents.

Table 7: Nanoindentation results of Mg-Zr coatings.

Coatings	Thickness (µm)	Max. Load (mN)	Max. Depth (nm)	Plastic Depth (nm)	Hardness (GPa)	Reduced Young's Modulus (GPa)	Young's Modulus (GPa)	H/E
Mg-0.0Zr	2.2	1.5	193.8	181.9	1.4±0.1	79±6	78±6	0.02
Mg-0.4Zr	2.5	1.5	233.4	223.1	1.0±0.1	78±9	77±9	0.01
Mg-1.0Zr	2.7	1.5	211.7	201.5	1.2±0.1	86±7	85±7	0.01
Mg-2.0Zr	2.5	1.5	160.8	148.6	1.8±0.2	89±6	88±7	0.02
Mg-3.4Zr	2.4	1.5	151.7	139.1	1.9±0.1	91±8	90±9	0.02
Mg-5.0Zr	2.2	1.5	145.2	131.3	2.2±0.3	85±10	85±10	0.03

4.3. Corrosion behaviour

In order to investigate the corrosion behaviour of the Mg-Zr coatings, EIS and PP techniques were employed. The Tafel plot of the Mg-Zr coatings obtained from PP is depicted in figure 29. The PP test parameters are listed in Table 8. The results indicated a reduction in the corrosion rate of Mg-Zr coatings due to the doping effect of Zr on Mg, particularly in the Zr content range from 1.0 to 3.4 at.%. However, the corrosion rate significantly increased for the Mg-5.0Zr coating with the highest Zr content. In comparison, the corrosion rate was minimal for SS 316L due to its inherent corrosion-resistant properties. Mg-0.0Zr and Mg-0.4Zr coatings exhibited similar corrosion rates. By introducing Zr into the Mg matrix, the corrosion potential of Mg shifted towards the passive region (more positive), as evidenced by the E_{corr} values in Table 8.

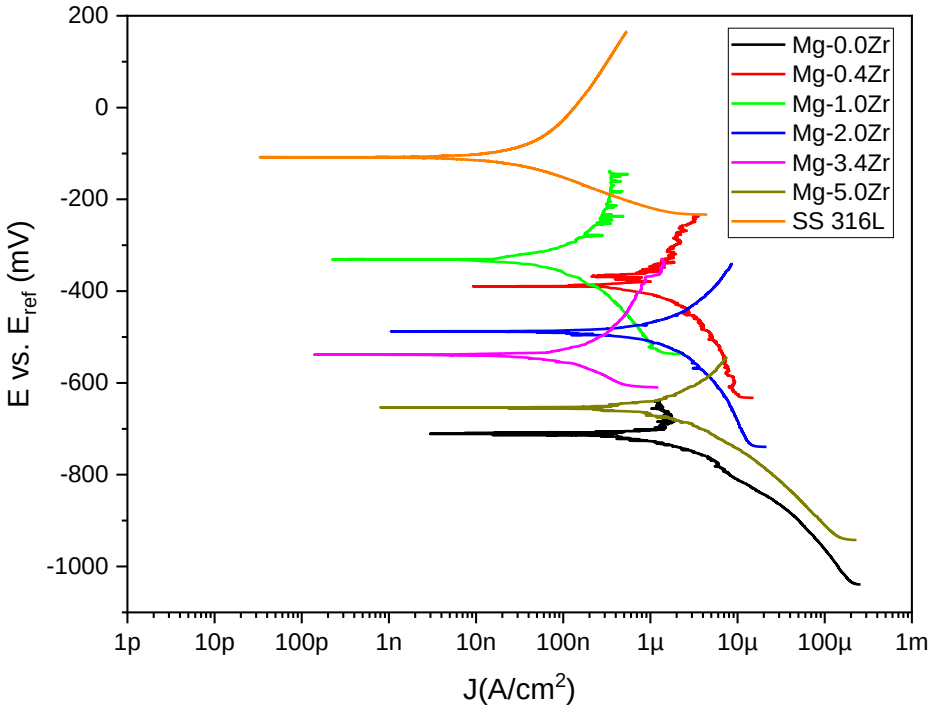

Figure 29: Tafel plot obtained from PP tests of the Mg-Zr coatings in plasma SBF solution.

Table 8: Parameters of PP tests after fitting.

Coatings	β_a (mV/decade)	β_c (mV/decade)	J_{corr} ($\mu A/cm^2$)	E_{corr} (mV)	CR ($\times 10^{-4}$) (mm/yr)
SS 316L	153±6	76±2	(3.38±0.41) $\times 10^{-5}$	-110±7	0.04±0.01
Mg-0.0Zr	57±38	40±1	1946±518	-714±3	8.39±2.23
Mg-0.4Zr	137±127	32±28	1916±1284	-426±36	8.33±5.58
Mg-1.0Zr	46±19	45±3	124±12	-356±24	0.54±0.05
Mg-2.0Zr	13±3	24±1	491±73	-458±31	2.09±0.31
Mg-3.4Zr	16±8	11±3	31±17	-525±14	0.13±0.07
Mg-5.0Zr	42±7	56±10	1275±657	-571±83	339.92±175.20

Figure 30 presents SEM images of Mg-Zr coatings after undergoing a corrosion test using PP. The SEM image provides further support for the results obtained from the PP test. Coating remnants were observed in the Mg-Zr coatings with Zr contents ranging from 1.0 to 3.4 at. % (Mg-1.0Zr, Mg-2.0Zr, and Mg-3.4Zr), as shown in figures 30c, 30d, and 30e. However, Mg-0.0Zr, Mg-0.4Zr, and Mg-5.0Zr coatings, which had the lowest and highest Zr amounts, exhibited minimal coating presence. Figure 31, figure 32 and figure 33 displays EDS scan for Mg-1.0Zr, Mg-2.0Zr and Mg-3.4Zr coatings respectively, indicating that the corrosion products mainly consist of Mg and Zr oxides. Additionally, elements such as sodium, phosphorous, and calcium were present, likely originating from plasma SBF solutions. This observation indicates that the corrosion by-products primarily consisted of hydroxides, phosphates, and carbonates, which originated from the reaction between hydroxide ions (OH^-) and HCO_3^- and HPO_4^{-2} species present in the plasma SBF. Consequently, this reaction led to the formation of insoluble carbonates and phosphates through precipitation [76].

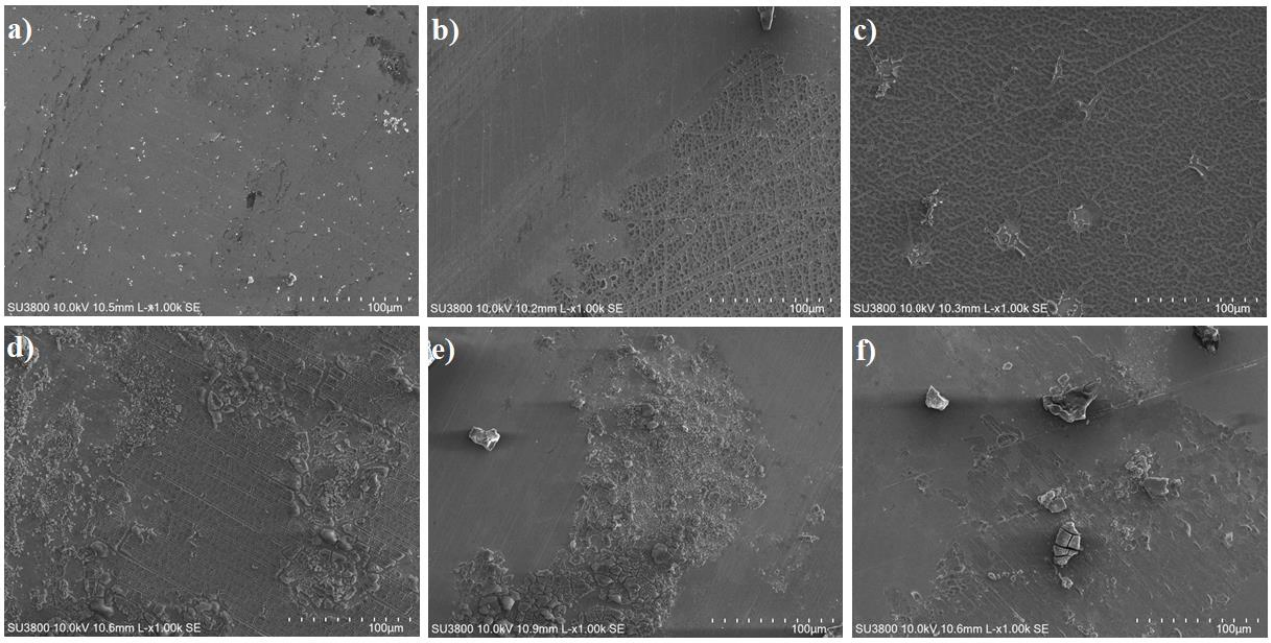

Figure 30: SEM images of the Mg-Zr coatings after corrosion test in plasma SBF solution: a) Mg-0.0Zr; b) Mg-0.4Zr; c) Mg-1.0Zr; d) Mg-2.0Zr; e) Mg-3.4Zr; and f) Mg-5.0Zr.

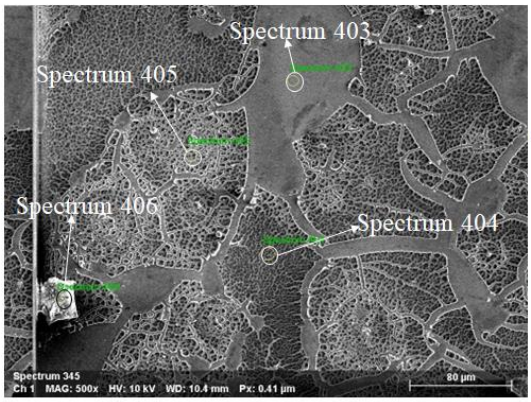

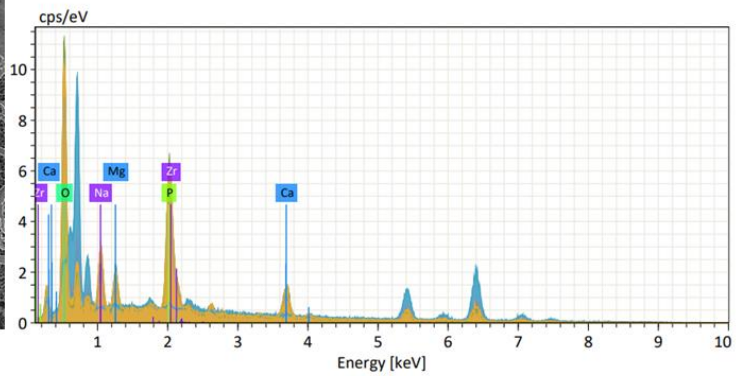

Atomic concentration [%]

Spectrum	O	Na	Mg	P	Ca	Cr	Fe	Ni	Zr
Spectrum 403						17.9	72.8	9.3	
Spectrum 404	70.8	5.8	3.3	8.3	7.0				4.7
Spectrum 405	70.9	5.9	3.7	8.9	6.0				4.6
Spectrum 406	70.1	6.9	3.4	8.5	6.3				4.9
Mean	**70.6**	**6.2**	**3.5**	**8.6**	**6.5**	**17.9**	**72.8**	**9.3**	**4.8**
Sigma	**0.5**	**0.6**	**0.2**	**0.3**	**0.5**	**0.0**	**0.0**	**0.0**	**0.2**
Sigma Mean	**0.2**	**0.3**	**0.1**	**0.2**	**0.3**	**0.0**	**0.0**	**0.0**	**0.1**

Figure 31: SEM image and EDS scan of Mg-1.0Zr coating after PP corrosion test in plasma SBF.

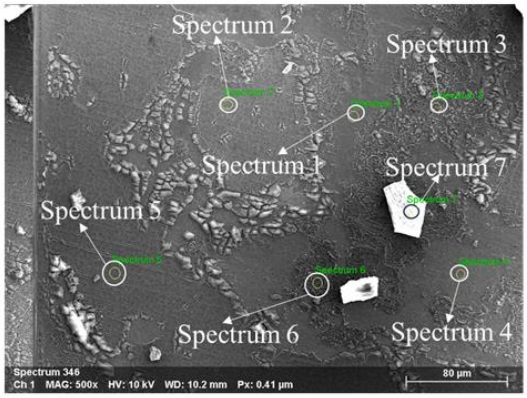

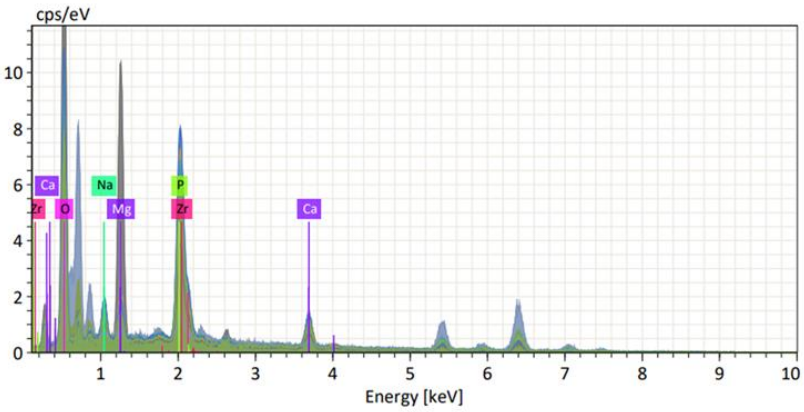

Atomic concentration [%]

Spectrum	O	Na	Mg	P	Ca	Cr	Fe	Ni	Zr
Spectrum 1	69.5	3.9	3.2	9.6	6.4				7.3
Spectrum 2	70.9	3.5	2.9	9.3	6.9				6.5
Spectrum 3	71.6	3.1	2.8	9.4	5.9				7.2
Spectrum 4						18.9	71.7	9.4	
Spectrum 5	70.5	3.7	3.2	9.5	6.3				6.8
Spectrum 6	71.6	1.6	17.2	3.9	2.5				3.2
Spectrum 7	68.9	2.8	3.0	10.1	7.4				7.9
Mean	**70.5**	**3.1**	**5.4**	**8.6**	**5.9**	**18.9**	**71.7**	**9.4**	**6.4**
Sigma	**1.1**	**0.9**	**5.8**	**2.4**	**1.7**	**0.0**	**0.0**	**0.0**	**1.6**
Sigma Mean	**0.4**	**0.3**	**2.2**	**0.9**	**0.7**	**0.0**	**0.0**	**0.0**	**0.6**

Figure 32: SEM image and EDS scan of Mg-2.0Zr coating after PP corrosion test in plasma SBF.

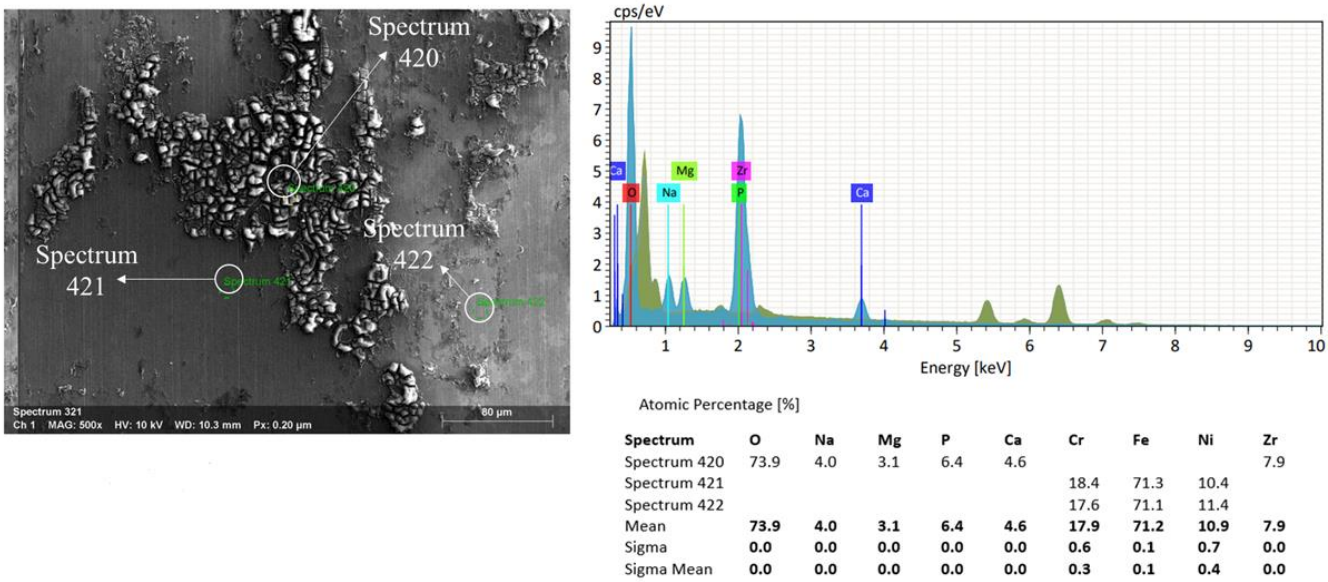

Atomic Percentage [%]

Spectrum	O	Na	Mg	P	Ca	Cr	Fe	Ni	Zr
Spectrum 420	73.9	4.0	3.1	6.4	4.6				7.9
Spectrum 421						18.4	71.3	10.4	
Spectrum 422						17.6	71.1	11.4	
Mean	**73.9**	**4.0**	**3.1**	**6.4**	**4.6**	**17.9**	**71.2**	**10.9**	**7.9**
Sigma	**0.0**	**0.0**	**0.0**	**0.0**	**0.0**	**0.6**	**0.1**	**0.7**	**0.0**
Sigma Mean	**0.0**	**0.0**	**0.0**	**0.0**	**0.0**	**0.3**	**0.1**	**0.4**	**0.0**

Figure 33: SEM image and EDS scan of Mg-3.4Zr coating after PP corrosion test in plasma SBF.

The EDS mapping of Mg-1.0Zr coating is shown in figure 34, which was obtained after the PP corrosion test. The mapping indicated the presence of an oxide layer on the surface of the coating, which can be either Zr or Mg oxides. Diplas et al. [77] suggested that the Zr hydroxide is more stable in an aqueous environment over a wide pH range and is thermodynamically stable compared to magnesium hydroxide ($Mg(OH)_2$), and hence zirconium hydroxide ($Zr(OH)_4$) was most probably responsible for the protection offered by Zr in Mg matrix. These oxides were mostly amorphous in nature. In addition, magnesium hydroxide was non-protective in chloride environments, as described by many authors [78].

However, Zr did not protect the coating when the amount of Zr was increased to 5.0 at.%. This might be due to Zr-rich particles in Mg matrix promoting galvanic corrosion where Zr particles acted as cathodes and α-Mg matrix acted as anodes, leading to severe corrosion. The EDS area mapping of Mg-1.0Zr also revealed non-uniform corrosion occurring in Mg-Zr coatings where columnar boundaries were preferential sites of attack by plasma SBF. The pitting corrosion that occurred on the surface of Mg alloy was due to attack by chloride ions, which attacked the $Mg(OH)_2$ layer and converted it into soluble magnesium chloride ($MgCl_2$) [76].Asta Griguceviciene et al. [79] also reported similar results in magnetron sputtered Mg-Al-Zr coatings, where increment of Zr led to structural inhomogeneity and electrochemical activity of the alloy with higher Zr content was higher than pure Mg. Walter et al. [80] reported an increased occurrence of pitting corrosion in Mg alloys with higher surface roughness. During the PP test, the Mg-2.0Zr coating exhibited a higher corrosion rate compared to Mg-1.0Zr and Mg-3.4Zr coatings. This behaviour can be attributed to the presence of deep valleys and higher surface roughness. Lin Sun et al. [74] also reported similar results, where an increase in surface roughness allowed electrolyte penetration into the inner metal layer through microscopic concave valley surfaces, resulting in surface corrosion of AZ31 Mg alloy treated by microarc fluorination.

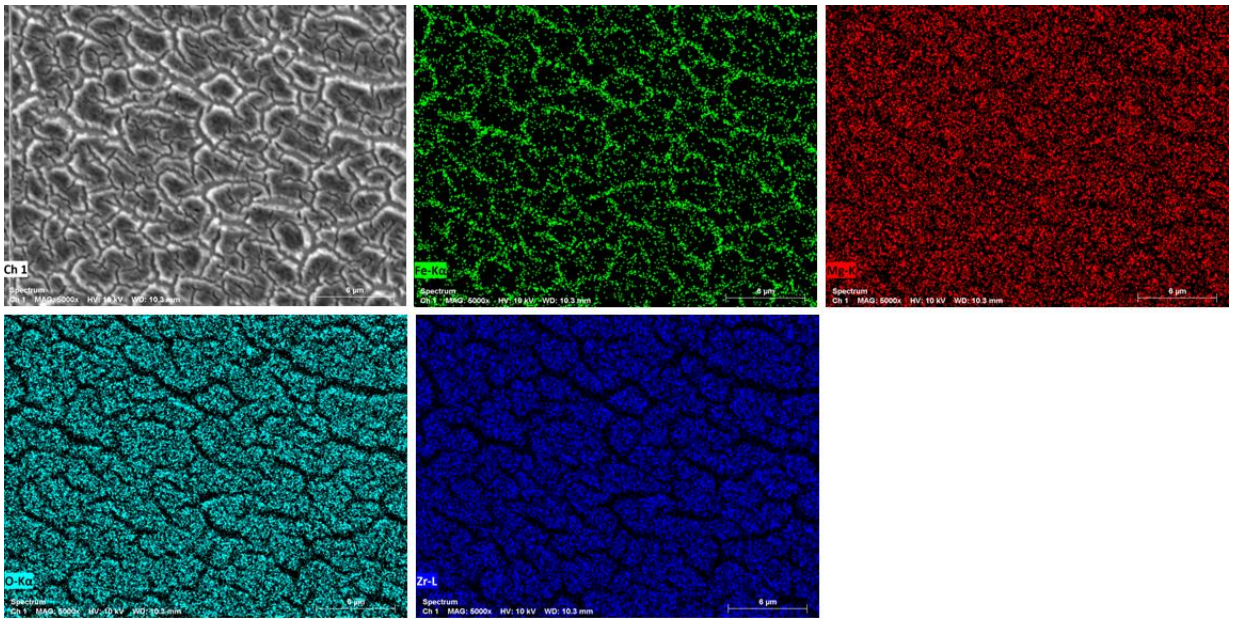

Figure 34: EDS mapping of the Mg-1.0 Zr coating after PP test in plasma SBF solution.

Initially, a preliminary test was conducted using EIS to determine the degradation time. The tests were performed on SS 316L and Mg-0.0Zr coating. Figure 35 presents a bode plot illustrating the charge transfer resistance and phase angle of the film at 24 and 48 hours. The results indicated that both Mg-0.0Zr and SS 316L exhibited similar behaviour after 24 hours, suggesting complete film degradation within that timeframe. Consequently, it was decided to conduct the experiment until time required for stabilization of OCP.

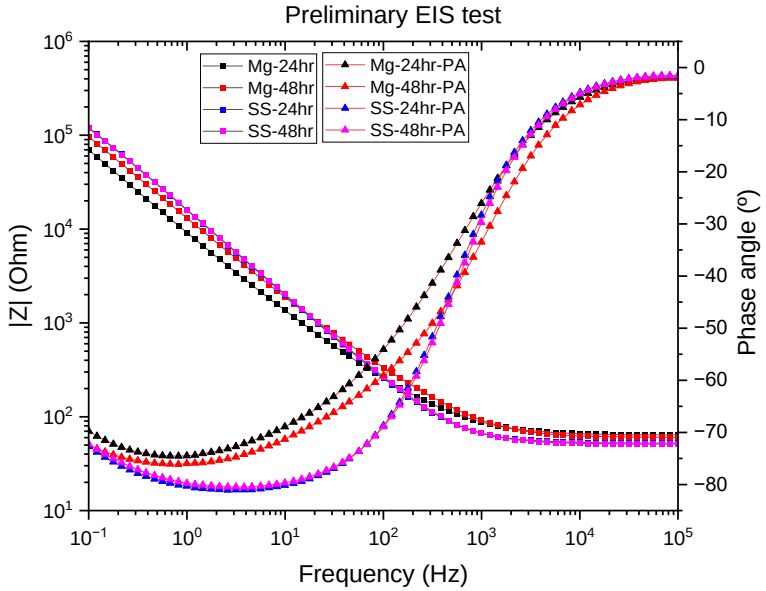

Figure 35: Bode plot of Mg-0.0Zr coating and SS 316L preliminary test in plasma SBF solution.

The results of all EIS experiments are listed in Table 9 and showed the presence of one time constant in electrochemical system. Figure 36 shows equivalent electric circuit diagram of simple Randles circuit. This was further supported by the Nyquist plot in figure 37, where there is a flattened semicircle, which was due to the presence of surface inhomogeneity caused by the non-uniform distribution of current flow. Due to this reason ideal capacitance was replaced by CPE [81]. The centre of the arc was represented by the resistance (R), and the radius of the arc was related to the time constant (τ) of the system. Upon analysing the Nyquist plot, it was observed that SS 316L did not depict a semicircle, indicating the absence of capacitive behaviour. This suggested that SS 316L did not possess a capacitive element.

The bode plot in figure 38 indicates charge transfer resistance at lower frequencies (R_{coat}) and solution resistance (R_{sol}) at higher frequencies, with capacitance represented by the constant phase element CPE at intermediate frequencies. This matched with the simple Randles circuit of an equivalent electric circuit diagram where there was single slope change at intermediate frequency which indicated presence of capacitance (CPE). Table 8 includes all the results obtained from fitting bode plots in Gamry software where the chi square is in the order of 10^{-3} which confirmed good fitting of the curve [82]. R_{coat} is the resistance of the coating, R_{sol} is the solution resistance, CPE is the value of the constant phase element, and α is the exponent of CPE. In the first column of Table 9, the R_{coat} value is extremely high for SS 316L, which indicated its resistance to corrosion in plasma SBF solution. However, there was no significant difference in the value of coating resistance (R_{coat}) for other compositions of the film. Surprisingly, the value of coating resistance was higher for Mg-0.0Zr and Mg-0.4Zr, which may be due to the formation of an oxide layer on the surface of the coatings, contributing to an increase in overall impedance. Mg-3.4Zr showed a higher value of coating resistance, supporting the results of PP test. The solution resistance (R_{sol}) of Mg-0.0Zr was higher compared to other coatings, indicating its higher degradation rate in plasma SBF solution, which clearly reflected its poor corrosion resistance in chloride environments of plasma SBF solution.

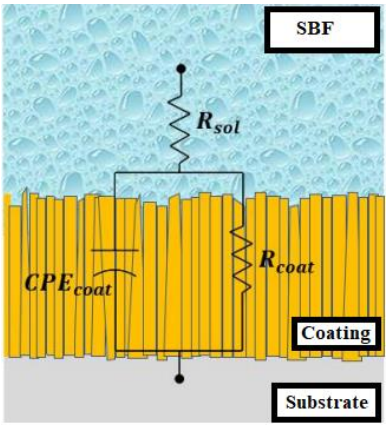

Figure 36: Equivalent Electric Circuit of the Mg-Zr coatings, image adapted from [71].

The value of the exponent of CPE ranges from 0 to 1. A value close to 1 signifies that the material behaves as a pure capacitor, and a value close to 0 indicates that the material possesses defects and impurities and behaves more like resistance [71]. SS 316L behaved

more like a capacitor, with its value close to 1. In the case of the Mg-Zr coatings, Mg-(0.4–3.4) Zr possessed good capacitance behaviour. However, Mg-0.0Zr and Mg-5.0Zr exhibited poor capacitance behaviour compared to other Mg-Zr coatings.

Table 9: Parameters of EIS after fitting with equivalent electric circuit.

Coatings	**R_{coat}(Ω)**	**R_{sol}(Ω)**	**CPE (μS×s^2) (1×10^{-5})**	**α**	**chi. sq(1×10^{-3})**
SS 316L	(20.5±6.8) ×10^6	911±910	(9.9±2.5) ×10^{-6}	0.97±0.00	0.2±0.1
Mg-0.0Zr	1529±163	114±33	6.0±0.3	0.82±0.00	0.2±0.1
Mg-0.4Zr	1448±257	72±0.4	3.7±1.3	0.87±0.00	0.3±0.2
Mg-1.0Zr	1015±35	69±0.9	3.8±0.1	0.87±0.00	0.3±0.0
Mg-2.0Zr	1215±3	68±1.1	3.3±0.5	0.88±0.00	0.2±0.1
Mg-3.4Zr	1413±166	75±5.5	4.8±2.7	0.85±0.00	0.2±0.1
Mg-5.0Zr	1237±354	70±3.2	5.6±0.9	0.83±0.00	0.3±0.0

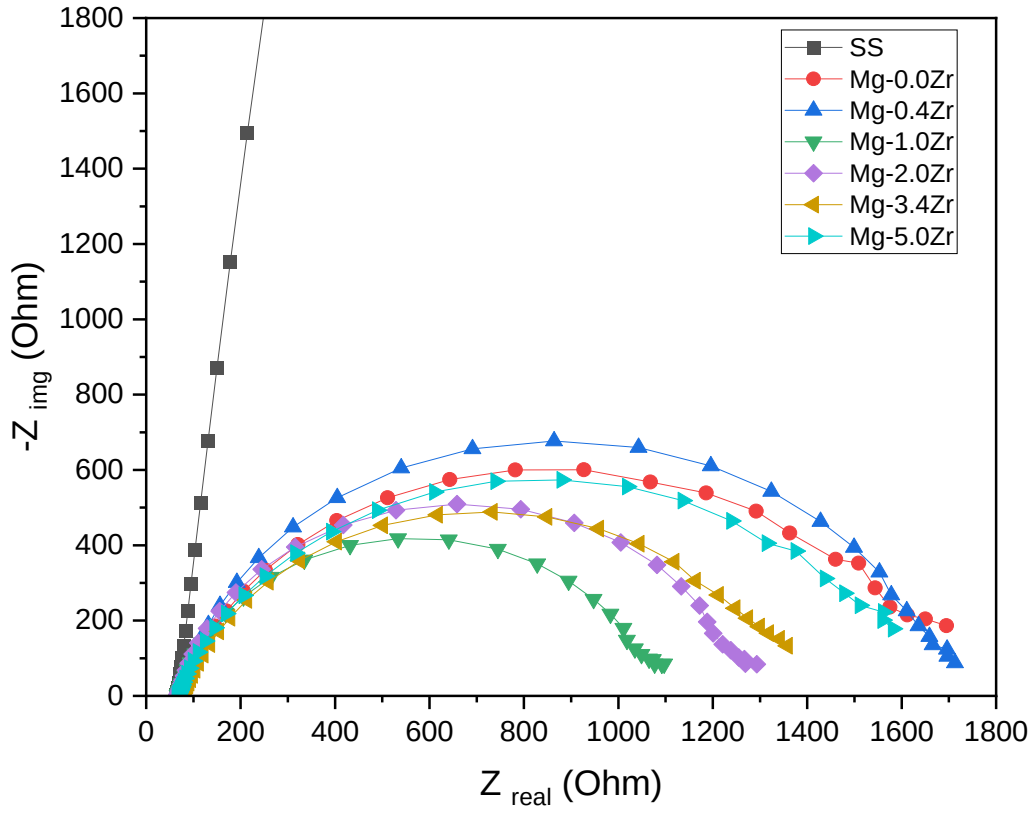

Figure 37: Nyquist plot of the Mg-Zr coatings in plasma SBF solution.

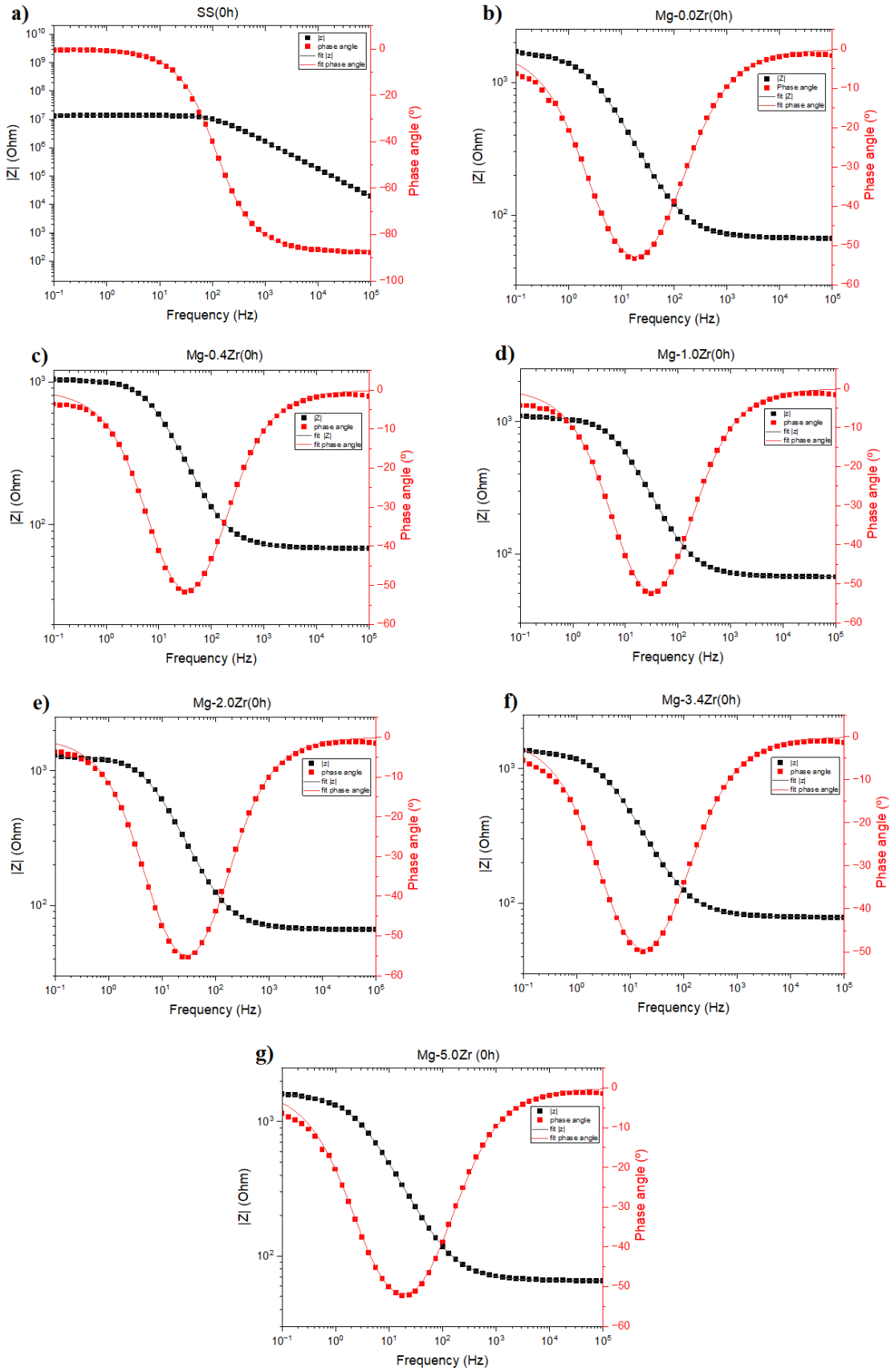

Figure 38: EIS bode plot of the Mg-Zr coatings and SS 316L substrate in plasma SBF solution: a) SS 316L; b) Mg-0.0Zr; c) Mg-0.4Zr; d) Mg-1.0Zr; e) Mg-2.0Zr; f) Mg-3.4Zr; and g) Mg-5.0 Zr.

Figure 39 illustrates the SEM results of the Mg-Zr coatings after the EIS test in a plasma SBF. These results supported the findings of the PP test, as remnants of coatings were observed in Mg-1.0Zr, Mg-2.0Zr, and Mg-3.4Zr, as shown in figure 39c, 39d, and 39e. Conversely, almost no coatings were observed in Mg-0.0Zr, Mg-0.4Zr, and Mg-5.0Zr, indicating a high corrosion rate for these coatings.

Figure 40 presents an EDS profile of the Mg-2.0Zr coating, displaying the chemical composition of the remaining portion of the coatings on the substrate. The results revealed the presence of O, Mg, and Zr in the remaining portion of the coating, indicating the presence of zirconium and magnesium oxides, with zirconium oxides being dominant. The corroded region exhibited elements such as Fe and Cr, which corresponded to the chemical composition of SS 316L. Surprisingly, elements such as Na, P, Ca, and Cl were also present, which originated from the plasma SBF solution. The presence of these elements further supported the results of the PP tests, indicating the bioactive nature of the coatings with plasma SBF.

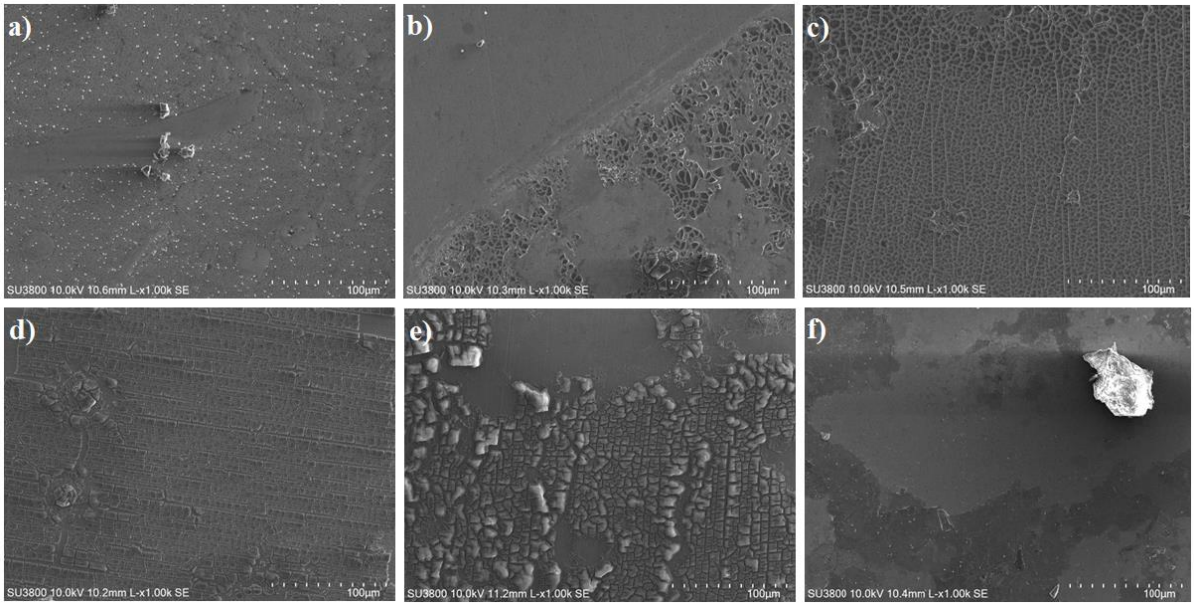

Figure 39: SEM images of the Mg-Zr coatings after EIS tests: a) Mg-0.0Zr; b) Mg-0.4Zr; c) Mg-1.0Zr; d) Mg-2.0Zr; e) Mg-3.4Zr; and f) Mg-5.0Zr.

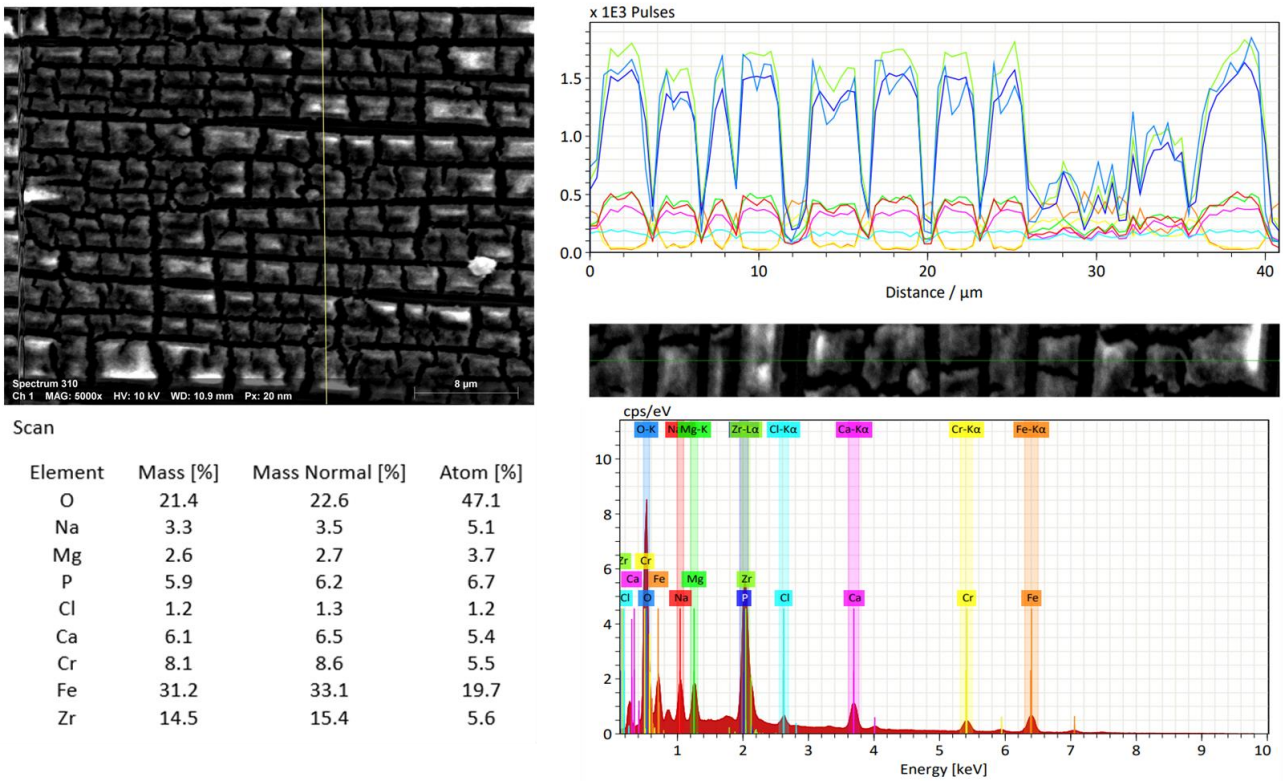

Scan

Element	Mass [%]	Mass Normal [%]	Atom [%]
O	21.4	22.6	47.1
Na	3.3	3.5	5.1
Mg	2.6	2.7	3.7
P	5.9	6.2	6.7
Cl	1.2	1.3	1.2
Ca	6.1	6.5	5.4
Cr	8.1	8.6	5.5
Fe	31.2	33.1	19.7
Zr	14.5	15.4	5.6

Figure 40: SEM image and EDS profile of the Mg-2.0Zr coating after EIS test.

4.4. Tribological behaviour

The tribological behaviour of the Mg-Zr coatings was evaluated by determining the COF and specific wear rate using a reciprocating tribometer. All tests were conducted under dry conditions, and the results were compared with an uncoated substrate (SS 316L). Initially, a preliminary test was performed for 10 minutes to assess the wear and frictional behaviour. However, the results indicated that the wear track depth exceeded the coating thickness, suggesting that the substrate was exposed during the test as shown in figure 41. Consequently, the test duration was reduced to 1 minute, during which the wear track depth was lower than the coating's thickness (~2 µm).

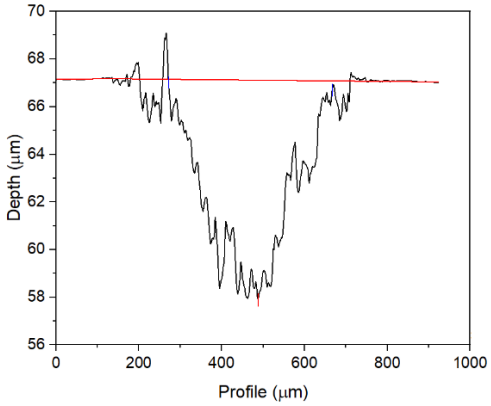

Figure 41: Wear track depth of the Mg-2.0Zr coating during preliminary test.

Figure 42 displays the COF of Mg-Zr coatings obtained from preliminary testing conducted under dry contact conditions. The graph depicts a "running in" period of approximately 200 seconds for all the coatings, during which the COF stabilizes and remains constant. After this running-in period, the COF shows a nearly identical value across all coatings and the substrate. This similarity in COF can be attributed to the failure of the coatings, resulting in the coatings encountering the substrate and producing a similar COF value. The average values of COF for preliminary test are mentioned in Table 10.

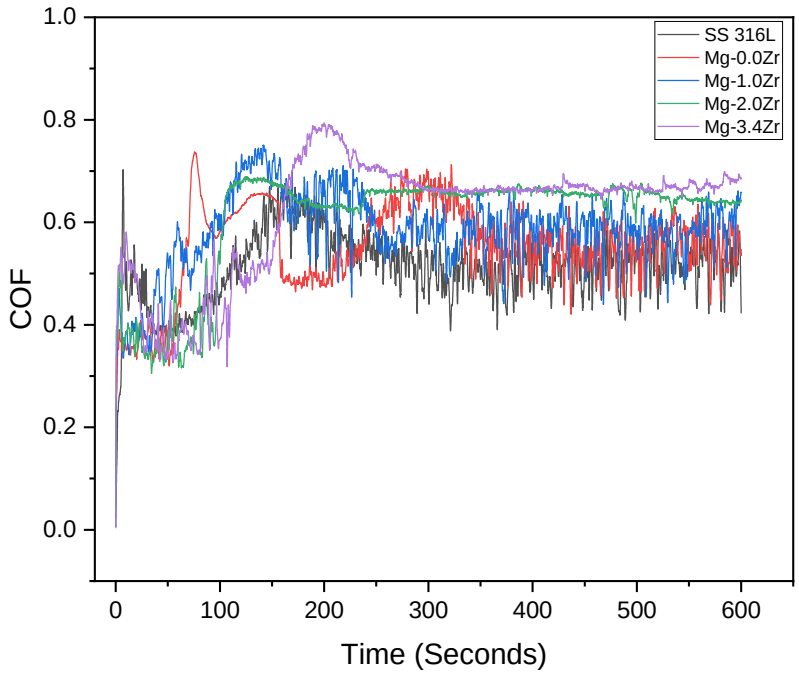

Figure 42: COF of the Mg-Zr coatings and substrate during preliminary reciprocating tests at 2 N.

Table 10: Average COF of the Mg-Zr coatings and substrate for preliminary test.

Samples	COF
SS 316L	0.53±0.01
Mg-0.0Zr	0.58±0.01
Mg-1.0Zr	0.57±0.00
Mg-2.0Zr	0.61±0.01
Mg-3.4Zr	0.63±0.01

Figure 43 depicts the COF of the 1-minute test. The graph illustrates a "running-in" period for the COF, which lasted approximately 10 seconds. After this period, the COF stabilized, and the values from this steady region were considered for calculation. The results indicated that the COF of the coatings was lower compared to the uncoated substrate.

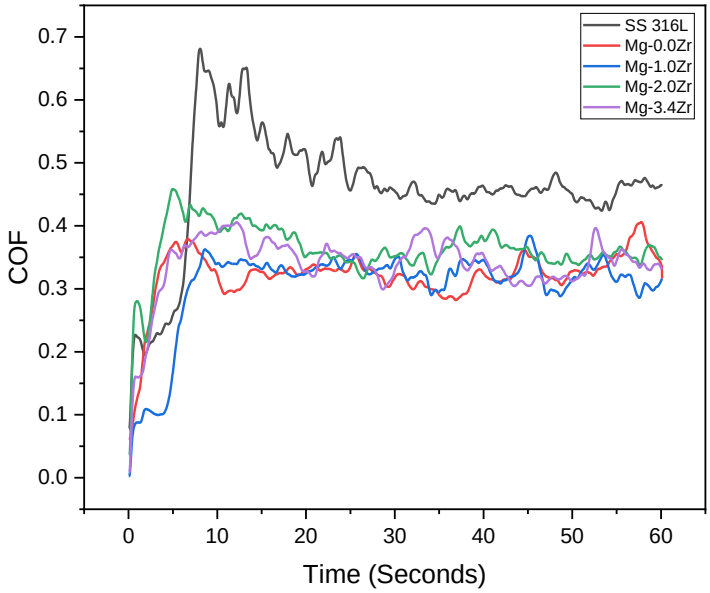

Figure 43: COF of the Mg-Zr coatings during reciprocating tests at 2 N load.

Table 10 provides the average COF values of the tested coatings, as well as the COF of the substrate. These values were obtained after three tribological under dry conditions for each case. The results showed no significant difference in average COF between pure magnesium and Zr-doped coatings. However, the average COF of the Mg-2.0Zr coating was slightly higher than that of the other coatings, potentially attributed to its higher surface roughness (27 nm).

Table 11: Average COF of the Mg-Zr coatings and substrate.

Samples	COF
SS 316L	0.47±0.01
Mg-0.0Zr	0.33±0.01
Mg-1.0Zr	0.33±0.00
Mg-2.0Zr	0.36±0.01
Mg-3.4Zr	0.34±0.01

Figure 44 displays the specific wear rate of the Mg-Zr coatings. The results demonstrated that the wear rate was high for all coatings. Among the coatings, Mg-3.4Zr exhibited a lower wear rate, whereas Mg-1.0Zr displayed a higher wear rate. This discrepancy could be attributed to the influence of hardness, as Mg-3.4Zr exhibited a higher hardness (1.9 GPa) compared to the Mg-1.0Zr and Mg-2.0Zr coatings. However, the wear rate of Mg-1.0Zr was even higher than that of Mg-0.0Zr, potentially due to the lower hardness of Mg-1.0Zr (1.2 GPa) in comparison to pure magnesium (1.4 GPa). As expected, the wear rate of the substrate (SS 316L) was lower due to its superior mechanical properties. The wear rate of the Mg-Zr coatings was high (in order of 10^{-3}) which showed their poor tribological behaviour. Figure 45 shows the wear tracks of the Mg-Zr coatings where there was formation of wide grooves on the surface of the coatings during tribological tests. The wear mechanism of the Mg-Zr coatings was abrasive wear as there was

formation of wide wear grooves on the surface of the coatings. Paul McGhee et al. [83] also reported similar results for average COF and wear volume for pure Mg and Mg alloys where the dominant mechanism of wear was abrasion.

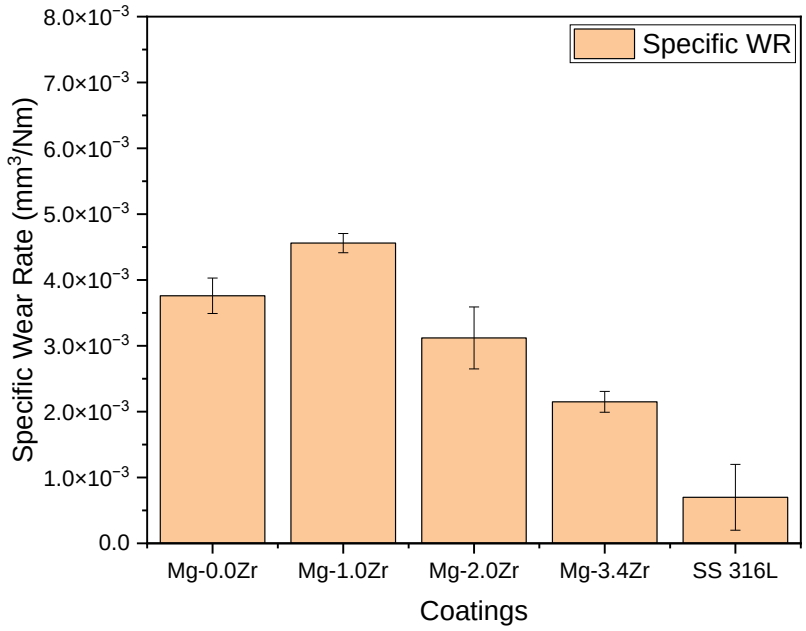

Figure 44: Specific wear rate of the Mg-Zr coatings and substrate under dry conditions.

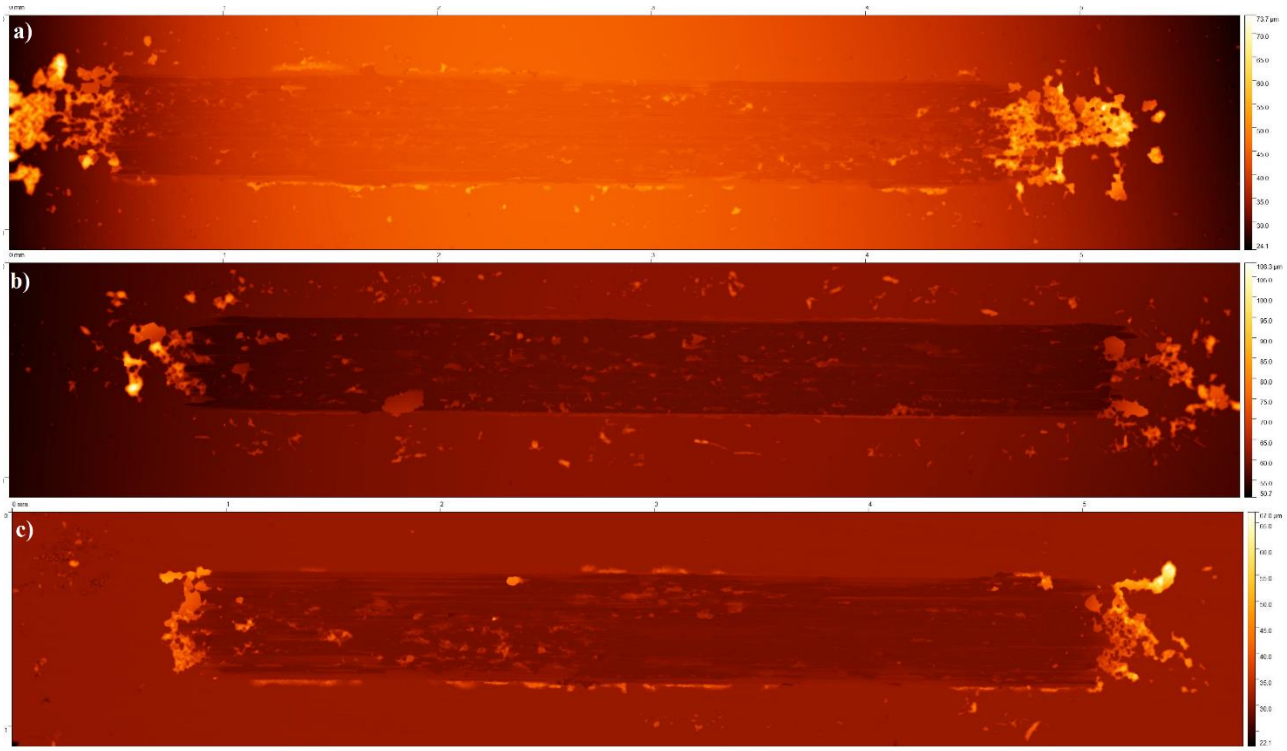

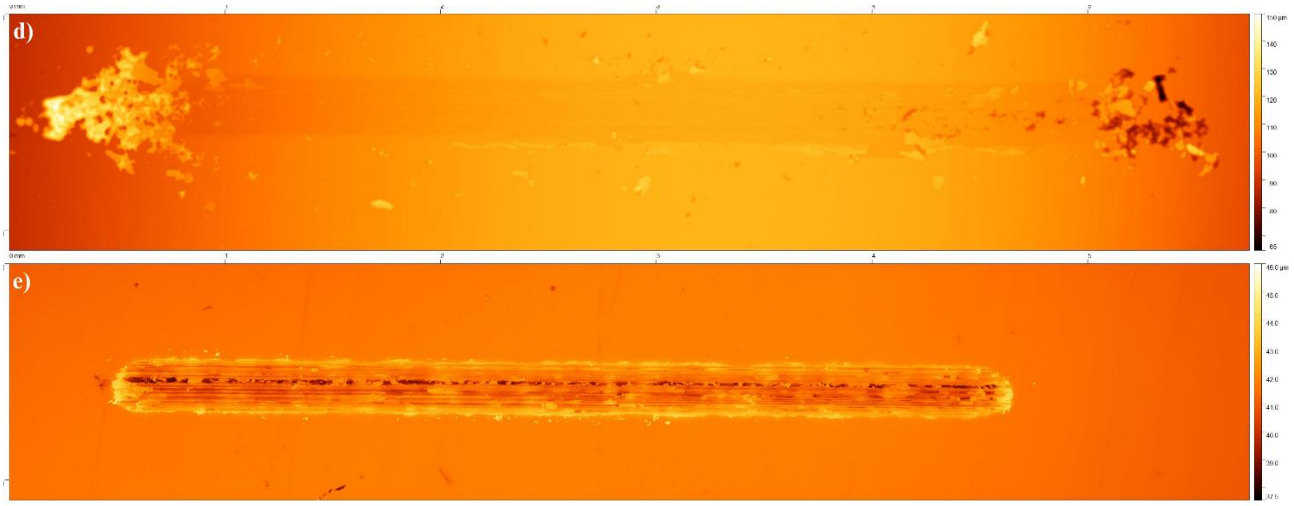

Figure 45: Wear track of the Mg-Zr coatings and substrate: a) Mg-0.0Zr; b) Mg-1.0Zr; c) Mg-2.0Zr; d) Mg-3.4Zr; and e) SS 316L.

5. Conclusions

Corrosion resistant Mg-Zr coatings for biodegradable and biocompatible temporary bone implants were successfully deposited using DCMS. Multiple characterization techniques were employed to analyse the morphological, chemical, structural, surface, electrochemical, and tribological properties of the coatings. The main findings of the study are as follows:

a. The incorporation of Zr into the Mg matrix resulted in refined columnar boundaries and slightly more compact coatings with fewer voids compared to pure magnesium. However, the overall coatings' morphology, characterized by columnar growth with hexagonal shapes at the top of the columns, remained similar for all coatings except pure magnesium, which exhibited a flake-like structure.
b. X-ray diffraction analysis revealed a dominant hexagonal Mg crystal structure, with the (00.2) plane becoming more prominent with increasing Zr content, while the (10.2) plane is dominant for the pure Mg coatings. The XRD peaks shifted to higher angles with increasing Zr content, indicating distortion of the crystal lattice due to the smaller atomic size of Zr. This distortion led to a decrease in the "c" lattice parameter, an increase in the "a" lattice parameter, and a reduction in interplanar spacing "d". The addition of Zr also resulted in a smaller crystallite size, confirming the grain-refining effect of Zr in the Mg matrix.
c. Contact angle measurements indicated that all the coatings under study exhibited a "liquiphilic" behaviour with contact angles less than 90º for the different liquids tested, in particular with plasma SBF. The Mg-1.0Zr coating showed a higher surface free energy, which decreased with increasing Zr content.
d. Surface roughness was highest for the Mg-0.4Zr and Mg-2.0Zr coatings, which exhibited deep valleys, while it decreased with increasing further the Zr content.
e. The hardness increased with the addition of Zr. However, Mg-0.4Zr and Mg-1.0Zr coatings displayed lower hardness compared to Mg-0.0Zr, possibly due to a high deposition rate leading to the formation of voids and less compact films. Regarding the Young's modulus, the addition of Zr did not have a significant influence. The hardness-to-elastic modulus ratio (H/E) was higher for Mg-5.0Zr coating (0.03) and lower for Mg-0.4Zr and Mg-1.0Zr (0.01).
f. The PP test demonstrated a reduced corrosion rate for Mg-1.0Zr, Mg-2.0Zr, and Mg-3.4Zr coatings in the plasma SBF environment. In contrast, the corrosion rate was high for Mg-0.0Zr, Mg-0.4Zr, and Mg-5.0Zr coatings. The obtained results were supported by SEM images, which revealed that Mg-5.0Zr exhibited the highest corrosion rate. This observation can be attributed to the initiation of galvanic corrosion resulting from the inhomogeneous distribution of Zr particles within the Mg matrix, with α-Mg acting as the anode and Zr particles serving as the cathode. EDS mapping confirmed the presence of magnesium and zirconium oxide, indicating that the Zr oxides may have acted as a protective layer against the electrolyte.
g. Electrochemical analyses were conducted using EIS and PP techniques. EIS measurements showed that the coatings behaved as a simple Randles circuit in the equivalent electric circuit diagram. Among the Mg-Zr coatings, Mg-(0.4–3.4) Zr

exhibited good capacitance behaviour, while Mg-0.0Zr and Mg-5.0Zr exhibited poor capacitance behaviour compared to the other coatings.

h. The tribological behaviour of Mg-Zr coatings, was found to be poor due to high wear rate. However, it is worth noting that the average COF of the coatings was lower compared to the SS 316L substrate. The incorporation of Zr resulted in a reduction of the wear rate, where Mg-3.4Zr coating exhibited a lower specific wear rate compared to the other Mg-Zr coatings. The wear mechanism observed was abrasive in nature.

In summary, the addition of Zr to the Mg matrix significantly improved the corrosion resistance in the region between 1.0 and 3.4 at. % Zr in the plasma SBF environment, making it a promising material for the development of biodegradable and biocompatible temporary bone implants. Zirconium also enhanced the mechanical properties and wear resistance of pure magnesium. Consequently, this composition holds potential for further development in bulk form using 3D printing techniques for temporary bone implants.

5.1. Future work

The successful deposition of Mg-Zr coatings using DC magnetron sputtering has assisted for further research and expansion of this study. However, there are several tasks that can be explored to enhance the scope of this work. Advanced characterization technique such as XPS can be employed to analyse presence of oxide and quantify their impact on the coatings. Additionally, refining the tribological testing parameters to closely simulate real-world operating conditions, resembling the environment of the human body, would enhance the accuracy and relevance of the results. It is important to note that the current study conducted tribological testing under dry conditions at room temperature, which may not fully represent the actual conditions experienced in practical applications.

To further advance the research, it is recommended to investigate Mg-Zr chemical compositions that demonstrate optimum corrosion behaviour, such as Mg-1.0Zr, Mg-2.0Zr, and Mg-3.4Zr, in bulk form using 3D printing techniques. This approach would enable a more comprehensive exploration of the Zr content range between 1.0 and 3.4 at.%. It is worth investigating the incorporation of Zn into Mg, and the subsequent development of Mg-Zr-Zn coatings, to examine the influence of Zn on the corrosion and tribological behaviour of Mg.

6. Bibliography

[1] M. P. Staiger, A. M. Pietak, J. Huadmai, and G. Dias, “Magnesium and its alloys as orthopedic biomaterials: A review,” *Biomaterials*, vol. 27, no. 9. pp. 1728–1734, Mar. 2006. doi: 10.1016/j.biomaterials.2005.10.003.

[2] H. Waizy *et al.*, “Biodegradable magnesium implants for orthopedic applications,” *Journal of Materials Science*, vol. 48, no. 1. pp. 39–50, Jan. 2013. doi: 10.1007/s10853-012-6572-2.

[3] J. Tan and S. Ramakrishna, “Applications of magnesium and its alloys: A review,” *Applied Sciences*, vol. 11, no. 15. MDPI AG, Aug. 01, 2021. doi: 10.3390/app11156861.

[4] H. Windhagen *et al.*, “Biodegradable magnesium-based screw clinically equivalent to titanium screw in hallux valgus surgery: Short term results of the first prospective, randomized, controlled clinical pilot study,” *Biomedical Engineering Online*, vol. 12, no. 1, Jul. 2013, doi: 10.1186/1475-925X-12-62.

[5] M. K. Kulekci, “Magnesium and its alloys applications in automotive industry,” *International Journal of Advanced Manufacturing Technology*, vol. 39, no. 9–10, pp. 851–865, Nov. 2008, doi: 10.1007/s00170-007-1279-2.

[6] H. Somekawa, “Effect of alloying elements on fracture toughness and ductility in Magnesium Binary Alloys; A Review,” *Materials Transactions*, vol. 61, no. 1. Japan Institute of Metals (JIM), pp. 1–13, 2020. doi: 10.2320/matertrans.MT-M2019185.

[7] L. A. Dobrzan´ski, D. Dobrzan´ski, G. E. Totten, and M. Bamberger, “The Importance of Magnesium and Its Alloys in Modern Technology and Methods of Shaping Their Structure and Properties.”

[8] Y. Chen, Z. Xu, C. Smith, and J. Sankar, “Recent advances on the development of magnesium alloys for biodegradable implants,” *Acta Biomaterialia*, vol. 10, no. 11. Elsevier Ltd, pp. 4561–4573, Nov. 01, 2014. doi: 10.1016/j.actbio.2014.07.005.

[9] N. Miguel Matias Mendes Bexiga et al., “Biocompatible Coatings for Functionalization of Magnesium Alloys in Biomedical Applications,” 2018.

[10] B. L. Mordike and T. Ebert, “Magnesium Properties-applications-potential,” 2001. [Online]. Available: www.elsevier.com/locate/msea

[11] M. Gupta, “Utilizing Magnesium based Materials to Reduce Green House Gas Emissions in Aerospace Sector,” *Aeronautics and Aerospace Open Access Journal*, vol. 1, no. 1, Jun. 2017, doi: 10.15406/aaoaj.2017.01.00005.

[12] B. R. Powell, P. E. Krajewski, and A. A. Luo, “Magnesium alloys for lightweight powertrains and automotive structures,” in *Materials, Design and Manufacturing for Lightweight Vehicles*, Elsevier, 2021, pp. 125–186. doi: 10.1016/b978-0-12-818712-8.00004-5.

[13] F. Witte, “The history of biodegradable magnesium implants: A review,” *Acta Biomaterialia*, vol. 6, no. 5. Elsevier Ltd, pp. 1680–1692, 2010. doi: 10.1016/j.actbio.2010.02.028.

[14] J. Durlach, “Overview of Magnesium Research: History and Current Trends.” Available: https://link.springer.com/chapter/10.1007/978-1-84628-483-0_1, Accessed on: May 51 2023.

[15] “History of Magnesia 1.1 History of Magnesia.” Available: https://catalogimages.wiley.com/images/db/pdf/0471656038.01.pdf, Accessed on: April 2023

[16] S. Kamrani and C. Fleck, “Biodegradable magnesium alloys as temporary orthopaedic implants: a review,” *BioMetals*, vol. 32, no. 2. Springer Netherlands, pp. 185–193, Apr. 01, 2019. doi: 10.1007/s10534-019-00170-y.

[17] P. C. Banerjee, S. Al-Saadi, L. Choudhary, S. E. Harandi, and R. Singh, “Magnesium implants: Prospects and challenges,” *Materials*, vol. 12, no. 1. MDPI AG, Jan. 03, 2019. doi: 10.3390/ma12010136.

[18] G. Manivasagam and S. Suwas, “Biodegradable Mg and Mg based alloys for biomedical implants,” *Materials Science and Technology*, vol. 30, no. 5. Maney Publishing, pp. 515–520, 2014. doi: 10.1179/1743284713Y.0000000500.

[19] Y. Yang *et al.*, “Mg bone implant: Features, developments and perspectives,” *Materials and Design*, vol. 185. Elsevier Ltd, Jan. 05, 2020. doi: 10.1016/j.matdes.2019.108259.

[20] S. Nayak, B. Bhushan, R. Jayaganthan, P. Gopinath, R. D. Agarwal, and D. Lahiri, “Strengthening of Mg based alloy through grain refinement for orthopaedic application,” *Journal Mechanical Behaviour Biomedical Material*, vol. 59, pp. 57–70, Jun. 2016, doi: 10.1016/j.jmbbm.2015.12.010.

[21] S. Balasubramanian, “Magnetron sputtered magnesium-based thin film metallic glasses for bioimplants,” *Biointerphases*, vol. 16, no. 1, p. 011005, Jan. 2021, doi: 10.1116/6.0000535.

[22] H. Zhou *et al.*, “Influence of Zirconium (Zr) on the microstructure, mechanical properties and corrosion behaviour of biodegradable zinc-magnesium alloys,” *Journal Alloys Compound*, vol. 840, Nov. 2020, doi: 10.1016/j.jallcom.2020.155792.

[23] T. Ren *et al.*, “Evaluation of as-extruded ternary Zn–Mg–Zr alloys for biomedical implantation material: In vitro and in vivo behaviour,” *Materials and Corrosion*, vol. 70, no. 6, pp. 1056–1070, Jun. 2019, doi: 10.1002/maco.201810648.

[24] Y. C. Li, C. S. Wong, C. Wen, and P. D. Hodgson, “Biodegradable Mg-Zr-Ca alloys for bone implant materials,” *Materials Technology*, vol. 27, no. 1, pp. 49–51, Feb. 2012, doi: 10.1179/175355511X13240279339482.

[25] G. Song, “Control of biodegradation of biocompatible magnesium alloys,” *Corrosion Science*, vol. 49, no. 4. pp. 1696–1701, Apr. 2007. doi: 10.1016/j.corsci.2007.01.001.

[26] H. Feng *et al.*, “Systematic Study of Inherent Antibacterial Properties of Magnesium-based Biomaterials,” *ACS Applied Material Interfaces*, vol. 8, no. 15, pp. 9662–9673, Apr. 2016, doi: 10.1021/acsami.6b02241.

[27] K. Schlüter, C. Zamponi, N. Hort, K. U. Kainer, and E. Quandt, “Polycrystalline and amorphous MgZnCa thin films,” *Corrosion Science*, vol. 63, pp. 234–238, Oct. 2012, doi: 10.1016/j.corsci.2012.06.005.

[28] Y. Yang *et al.*, “Mg bone implant: Features, developments and perspectives,” *Materials and Design*, vol. 185. Elsevier Ltd, Jan. 05, 2020. doi: 10.1016/j.matdes.2019.108259.

[29] A. Atrens, S. Johnston, Z. Shi, and M. S. Dargusch, “Viewpoint - Understanding Mg corrosion in the body for biodegradable medical implants,” *Scriptia Materialia*, vol. 154, pp. 92–100, Sep. 2018, doi: 10.1016/j.scriptamat.2018.05.021.

[30] H. Li, Y. Zheng, and L. Qin, “Progress of biodegradable metals,” *Progress in Natural Science: Materials International*, vol. 24, no. 5. Elsevier B.V., pp. 414–422, Oct. 01, 2014. doi: 10.1016/j.pnsc.2014.08.014.

[31] R. Kumar and P. Katyal, “Effects of alloying elements on performance of biodegradable magnesium alloy,” *Material Today Proceedings*, vol. 56, pp. 2443–2450, Jan. 2022, doi: 10.1016/j.matpr.2021.08.233.

[32] M. Park, J. E. Lee, C. G. Park, S. H. Lee, H. K. Seok, and Y. bin Choy, “Polycaprolactone coating with varying thicknesses for controlled corrosion of magnesium,” *Journal Coating Technology Res*, vol. 10, no. 5, pp. 695–706, 2013, doi: 10.1007/s11998-013-9474-6.

[33] Y. Zhang *et al.*, “A study of degradation resistance and cytocompatibility of super-hydrophobic coating on magnesium,” *Materials Science and Engineering C*, vol. 78, pp. 405–412, Sep. 2017, doi: 10.1016/j.msec.2017.04.057.

[34] M. Sankar, S. Suwas, S. Balasubramanian, and G. Manivasagam, “Comparison of electrochemical behavior of hydroxyapatite coated onto WE43 Mg alloy by electrophoretic and pulsed laser deposition,” *Surface Coating Technology*, vol. 309, pp. 840–848, Jan. 2017, doi: 10.1016/j.surfcoat.2016.10.077.

[35] M. Razavi *et al.*, “Controlling the degradation rate of bioactive magnesium implants by electrophoretic deposition of akermanite coating,” *Ceramics International*, vol. 40, no. 3, pp. 3865–3872, Apr. 2014, doi: 10.1016/j.ceramint.2013.08.027.

[36] Y. Chen, Y. Song, S. Zhang, J. Li, C. Zhao, and X. Zhang, “Interaction between a high purity magnesium surface and PCL and PLA coatings during dynamic degradation,” *Biomedical Materials*, vol. 6, no. 2, 2011, doi: 10.1088/1748-6041/6/2/025005.

[37] C. Shuai, B. Wang, Y. Yang, S. Peng, and C. Gao, “3D honeycomb nanostructure-encapsulated magnesium alloys with superior corrosion resistance and mechanical properties,” *Composites PartB Engineering*, vol. 162, pp. 611–620, Apr. 2019, doi: 10.1016/j.compositesb.2019.01.031.

[38] S. Agarwal, J. Curtin, B. Duffy, and S. Jaiswal, “Biodegradable magnesium alloys for orthopaedic applications: A review on corrosion, biocompatibility and surface modifications,” *Materials Science and Engineering C*, vol. 68. Elsevier Ltd, pp. 948–963, Nov. 01, 2016. doi: 10.1016/j.msec.2016.06.020.

[39] Y. Li *et al.*, “Mg-Zr-Sr alloys as biodegradable implant materials,” *Acta Biomaterialia*, vol. 8, no. 8, pp. 3177–3188, 2012, doi: 10.1016/j.actbio.2012.04.028.

[40] Y. Ding, C. Wen, P. Hodgson, and Y. Li, “Effects of alloying elements on the corrosion behaviour and biocompatibility of biodegradable magnesium alloys: A review,” *Journal of Materials Chemistry B*, vol. 2, no. 14, pp. 1912–1933, Apr. 2014, doi: 10.1039/c3tb21746a.

[41] Y. L. Zhou *et al.*, “Microstructures and mechanical properties of as cast Mg-Zr-Ca alloys for biomedical applications,” *Materials Technology*, vol. 27, no. 1, pp. 52–54, Feb. 2012, doi: 10.1179/175355511X13240279340200.

[42] W. Zhang, M. Li, Q. Chen, W. Hu, W. Zhang, and W. Xin, “Effects of Sr and Sn on microstructure and corrosion resistance of Mg-Zr-Ca magnesium alloy for biomedical applications,” *Materials and Design*, vol. 39, pp. 379–383, 2012, doi: 10.1016/j.matdes.2012.03.006.

[43] D. Mushahary *et al.*, “Zirconium, calcium, and strontium contents in magnesium based biodegradable alloys modulate the efficiency of implant-induced osseointegration,” *International Journal of Nanomedicine*, vol. 8, pp. 2887–2902, Aug. 2013, doi: 10.2147/IJN.S47378.

[44] Y. Chen, J. Dou, H. Yu, and C. Chen, “Degradable magnesium-based alloys for biomedical applications: The role of critical alloying elements,” *Journal of Biomaterials Applications*, vol. 33, no. 10. SAGE Publications Ltd, pp. 1348–1372, May 01, 2019. doi: 10.1177/0885328219834656.

[45] M. S. Uddin, C. Hall, and P. Murphy, “Surface treatments for controlling corrosion rate of biodegradable Mg and Mg-based alloy implants,” *Science and Technology of Advanced Materials*, vol. 16, no. 5. Institute of Physics Publishing, Sep. 08, 2015. doi: 10.1088/1468-6996/16/5/053501.

[46] D. Raducanu *et al.*, “Mechanical Alloying Process Applied for Obtaining a New Biodegradable Mg-xZn-Zr-Ca Alloy,” *Metals*, vol. 12, no. 1, Jan. 2022, doi: 10.3390/met12010132.

[47] R. P. Verma, “Titanium based biomaterial for bone implants: A mini review,” in *Materials Today: Proceedings*, Elsevier Ltd, 2020, pp. 3148–3151. doi: 10.1016/j.matpr.2020.02.649.

[48] I. Hoffmann, Y. T. Cheng, D. A. Puleo, G. Song, and R. A. Waldo, “Mg-Ti: A possible biodegradable, biocompatible, mechanically matched material for temporary implants,” in *Materials Research Society Symposium Proceedings*, 2011, pp. 111–115. doi: 10.1557/opl.2011.566.

[49] S. E. Harandi, M. Mirshahi, S. Koleini, M. H. Idris, H. Jafari, and M. R. A. Kadir, “Effect of calcium content on the microstructure, hardness and in-vitro corrosion behavior of biodegradable mg-ca binary alloy,” *Materials Research*, vol. 16, no. 1, pp. 11–18, Jan. 2013, doi: 10.1590/S1516-14392012005000151.

[50] Z. Li, X. Gu, S. Lou, and Y. Zheng, “The development of binary Mg-Ca alloys for use as biodegradable materials within bone,” *Biomaterials*, vol. 29, no. 10, pp. 1329–1344, Apr. 2008, doi: 10.1016/j.biomaterials.2007.12.021.

[51] N. Ikeo, M. Nishioka, and T. Mukai, “Fabrication of biodegradable materials with high strength by grain refinement of Mg–0.3 at.% Ca alloys,” *Materials Letters*, vol. 223, pp. 65–68, Jul. 2018, doi: 10.1016/j.matlet.2018.03.188.

[52] R. C. Zeng, W. C. Qi, H. Z. Cui, F. Zhang, S. Q. Li, and E. H. Han, “In vitro corrosion of as-extruded Mg-Ca alloys-The influence of Ca concentration,” *Corrosion Science*, vol. 96, pp. 23–31, Jul. 2015, doi: 10.1016/j.corsci.2015.03.018.

[53] E. Willbold *et al.*, “Effect of the addition of low rare earth elements (lanthanum, neodymium, cerium) on the biodegradation and biocompatibility of magnesium,” *Acta Biomaterialia*, vol. 11, no. 1, pp. 554–562, 2015, doi: 10.1016/j.actbio.2014.09.041.

[54] D. Liu *et al.*, “Influence of fine-grain and solid-solution strengthening on mechanical properties and in vitro degradation of WE43 alloy,” *Biomedical Materials*, vol. 9, no. 1, 2014, doi: 10.1088/1748-6041/9/1/015014.

[55] A. Behera and T. Theivasanthi, “Magnetron Sputtering Magnetron sputtering for development of nanostructured materials.”

[56] J. H. La, S. Y. Lee, and S. J. Hong, “Synthesis of Zn-Mg coatings using unbalanced magnetron sputtering and their corrosion resistance,” *Surface Coating Technology*, vol. 259, no. PA, pp. 56–61, Nov. 2014, doi: 10.1016/j.surfcoat.2014.07.006.

[57] A. Grigucevičiene, K. Leinartas, R. Juškenas, and E. Juzeliunas, “Structure and initial corrosion resistance of sputter deposited nanocrystalline Mg-Al-Zr alloys,” *Materials Science and Engineering A*, vol. 394, no. 1–2, pp. 411–416, Mar. 2005, doi: 10.1016/j.msea.2004.11.047.

[58] Experimental Module 2 Crystal Structure Determination. II: Hexagonal Structures.” Available: https://link.springer.com/chapter/10.1007/978-1-4899-0148-4_5, Accessed on: April 15,2023.

[59] Y. Ji, X. Yu, and H. Zhu, “Fabrication of mg coating on peek and antibacterial evaluation for bone application,” *Coatings*, vol. 11, no. 8, Aug. 2021, doi: 10.3390/coatings11081010.

[60] J. D. Castro, B. Pinto, F. Ferreira, R. Serra, and S. Carvalho, “Wettability and corrosion resistance of zirconium nitride films obtained via reactive high-power impulse magnetron sputtering,” *Journal of Vacuum Science & Technology A*, vol. 41, no. 2, p. 023106, Mar. 2023, doi: 10.1116/6.0002341.

[61] W. C. Oliver and G. M. Pharr, “Measurement of hardness and elastic modulus by instrumented indentation: Advances in understanding and refinements to methodology,” 2004. [Online]. Available: www.mrs.org/publications/jmr/policy.html

[62] T. Kokubo and H. Takadama, “How useful is SBF in predicting in vivo bone bioactivity?” *Biomaterials*, vol. 27, no. 15, pp. 2907–2915, 2006, doi: 10.1016/j.biomaterials.2006.01.017.

[63] “Standard Practice for Calculation of Corrosion Rates and Related Information from Electrochemical Measurements 1”, doi: 10.1520/G0102-89R15E01.

[64] J. da Silva Rodrigues, L. Marasca Antonini, A. A. da Cunha Bastos, J. Zhou, and C. de Fraga Malfatti, “Corrosion resistance and tribological behavior of ZK30 magnesium alloy coated by plasma electrolytic oxidation,” *Surface Coating Technology*, vol. 410, Mar. 2021, doi: 10.1016/j.surfcoat.2021.126983.

[65] “Standard Test Method for Linearly Reciprocating Ball-on-Flat Sliding Wear”. Available: https://www.scribd.com/document/515379729/G133# ,Accessed on: June 10,2023.

[66] J. A. Thornton, “The microstructure of sputter-deposited coatings,” 1986.

[67] E. Kusano, “Structure-Zone Modeling of Sputter-Deposited Thin Films: A Brief Review,” *Applied Science and Convergence Technology*, vol. 28, no. 6, pp. 179–185, Nov. 2019, doi: 10.5757/asct.2019.28.6.179.

[68] F. Moens, I. C. Schramm, S. Konstantinidis, and D. Depla, “On the microstructure of magnesium thin films deposited by magnetron sputtering,” *Thin Solid Films*, vol. 689, Nov. 2019, doi: 10.1016/j.tsf.2019.137501.

[69] M. Störmer, C. Blawert, H. Hagen, V. Heitmann, and W. Dietzel, “Structure and corrosion of magnetron sputtered pure Mg films on silicon substrates,” in *Plasma Processes and Polymers*, 2007. doi: 10.1002/ppap.200731405.

[70] S. Diplas, P. Tsakiropoulos, and R. M. D. Brydson, “Development of physical vapour deposited Mg-Zr alloys: Part 1 - Characterisation of as deposited alloys,” *Materials Science and Technology*, vol. 15, no. 12, pp. 1349–1357, 1999, doi: 10.1179/026708399101505473.

[71] B. Da Costa, L. Pinto, M. José, and D. Castro, “Development of multifunctional coatings for the naval industry.” Available: https://estudogeral.uc.pt/bitstream/10316/103146/1/Tese_BeatrizPinto_VF.pdf, Accessed on: June 25,2023.

[72] J. D. Castro, M. J. Lima, and S. Carvalho, “Wetting and corrosion properties of CuxOy films deposited by magnetron sputtering for maritime applications,” *Applied Surface Science*, vol. 584, May 2022, doi: 10.1016/j.apsusc.2022.152582.

[73] J. Wei *et al.*, “Influence of surface wettability on competitive protein adsorption and initial attachment of osteoblasts,” *Biomedical Materials*, vol. 4, no. 4, 2009, doi: 10.1088/1748-6041/4/4/045002.

[74] L. Sun *et al.*, “Surface characterization and corrosion resistance of biomedical AZ31 Mg alloy treated by microarc fluorination,” *Scanning*, vol. 2020, 2020, doi: 10.1155/2020/5936789.

[75] S. Y. Kuan, H. S. Chou, and J. C. Huang, “Mechanical characteristics of Mg-Cu-Zr thin film metallic glasses,” *Surface Coating Technology*, vol. 231, pp. 58–61, Sep. 2013, doi: 10.1016/j.surfcoat.2012.03.055.

[76] F. Kiani, J. Lin, A. Vahid, K. Munir, C. Wen, and Y. Li, “Mechanical and corrosion properties of extruded Mg–Zr–Sr alloys for biodegradable implant applications,” *Materials Science and Engineering A*, vol. 831, Jan. 2022, doi: 10.1016/j.msea.2021.142192.

[77] S. Diplas, P. Tsakiropoulos, and R. M. D. Brydson, “Development of physical vapour deposited Mg-Zr alloys: Part 3 - Comparison of alloying and corrosion behaviour in Mg-V and Mg-Zr physical vapour deposited alloys,” *Materials Science and Technology*, vol. 15, no. 12. Maney Publishing, pp. 1373–1378, 1999. doi: 10.1179/026708399101505491.

[78] K. Schlüter, C. Zamponi, A. Piorra, and E. Quandt, “Comparison of the corrosion behaviour of bulk and thin film magnesium alloys,” *Corrosion Science*, vol. 52, no. 12, pp. 3973–3977, Dec. 2010, doi: 10.1016/j.corsci.2010.08.011.

[79] A. Grigucevičiene, K. Leinartas, R. Juškenas, and E. Juzeliunas, “Structure and initial corrosion resistance of sputter deposited nanocrystalline Mg-Al-Zr alloys,” *Materials Science and Engineering A*, vol. 394, no. 1–2, pp. 411–416, Mar. 2005, doi: 10.1016/j.msea.2004.11.047.

[80] R. Walter and M. B. Kannan, “Influence of surface roughness on the corrosion behaviour of magnesium alloy,” *Materials and Design*, vol. 32, no. 4, pp. 2350–2354, Apr. 2011, doi: 10.1016/j.matdes.2010.12.016.

[81] S. Feliu, “Electrochemical impedance spectroscopy for the measurement of the corrosion rate of magnesium alloys: Brief review and challenges,” *Metals*, vol. 10, no. 6. MDPI AG, pp. 1–23, Jun. 01, 2020. doi: 10.3390/met10060775.

[82] G. I. Cubillos, E. Romero, and A. Umaña-Perez, “ZrN-ZrOxNy vs ZrO2-ZrOxNy coatings deposited via unbalanced DC magnetron sputtering,” *Sci Rep*, vol. 11, no. 1, Dec. 2021, doi: 10.1038/s41598-021-98052-2.

[83] P. McGhee, D. Pai, S. Yarmolenko, Z. Xu, S. Neralla, and Y. Chen, “Tribological study of magnesium alloys for implant applications,” 2014. [Online]. Available: http://www.asme.org/about-asme/terms-of-use